Determination of Mechanical Properties of Blood Vessels and Surgical Conduits Using Nonlinear Optimization Techniques

by

Samir Donmazov

A Dissertation Submitted to the
Graduate School of Sciences and Engineering
in Partial Fulfillment of the Requirements for
the Degree of

Master of Science

in

Mechanical Engineering

KOÇ UNIVERSITY

July 18, 2016

Determination of Mechanical Properties of Blood Vessels and Surgical Conduits Using Nonlinear Optimization Techniques

Koç University

Graduate School of Sciences and Engineering

This is to certify that I have examined this copy of a master's thesis by

Samir Donmazov

and have found that it is complete and satisfactory in all respects, and that any and all revisions required by the final examining committee have been made.

Committee Members:

Assoc. Prof. Kerem Pekkan

Prof. Metin Muradoğlu

Assoc. Prof. Hakan Ertürk

Date:

Abstract

Vascular growth and remodeling during embryonic development is associated with blood flow and pressure induced stress distribution, in which residual strains and stresses play a central role. Residual strains are typically measured by performing *in vitro* tests on the excised vascular tissue. In this study, we investigated the possibility of estimating residual strains and stresses using physiological pressure-radius data obtained through *in vivo* noninvasive measurement techniques, such as optical coherence tomography or ultrasound modalities.

As an application, vessel buckling occurs due to the mechanical instability in the structure of the material that is used as vascular conduit. Thus it is essential for surgeons to select appropriate buckling resistant materials for reconstructive surgeries. In this study, torsional buckling effect was examined on three different materials such as PTFE, Dacron and porcine pericardium, which are commonly used as vascular conduits, by using linear elastic model. In addition, nonlinear material properties of porcine pericardium and human pericardium were examined.

Finally a mechanical perspective for the optimization of living organisms may provide an understanding of the variation in mechanical properties and sizes of biological tissues including cardiovascular vessels, bones and cartilage, subjected to physiological mechanical loading. Thus in this study we proposed two different approaches to reveal the possible optimization scenarios in which either material properties (remodeling) or sizes (growth) of the arterial wall alter in order to make the stress distribution uniform close to homeostatic stresses as much as possible while the blood pressure increases.

Özet

Embyonik gelişim sırasında damar büyümesi ve yapısındaki değişimler kan akışının ve basıncının oluşturduğu gerilim dağılımı ile ilişkilidir ve bu gerilim dağılımda artık gerilimlerin (residual stresses) büyük rolü vardır. Artık şekil değiştirmeler (residual strains) genellikle canlı dışı (*in vitro*) deneylerle kesilmiş damar dokusu üzerinde ölçülür. Biz bu çalışmada artık gerilimlerin ve şekil değiştirmelerin optik koherens tomografi ve ultrason yöntemleri gibi canlı içi (*in vivo*) noninvazif ölçüm teknikleriyle elde edilen basınç-iç yarıçap verilerini kullanarak bulunması ihtimalini araştırdık.

Uyulama olarak, damar burkulması vasküler segment olarak kullanılan malzemenin yapısındaki mekaniksel dengesizlikten dolayı oluşur. Bu sebepten vasküler segment olarak burkulmaya dayanıklı uygun malzemelerin seçimi cerrahlar için çok önemlidir. Böylelikle, bu çalışmada vasküler segment olarak yaygın kullanılan PTFE, Dacron ve domuz perikardı gibi üç farklı malzeme üzerinde burulma ile oluşan burkulma etkilerini inceledik. İlaveten, domuz ve insan perikardlarının lineer olmayan malzeme özellikleri incelendi.

Canlı organizmaların optimizasyonu mekanik açısından değerlendirildiğinde kalp-damar dokusu, kemik, kıkırdak vs. gibi farklı mekaniksel yüklere maruz kalan biyolojik dokuların malzeme yapılarındaki ve boyutlarındaki değişimleri anlamakta aydınlatıcı bilgiler sunabilir. Böylece biz bu çalışmada arter duvarı boyunca gerilim dağılımını olabildiğince homeostatik gerilim değerlerine yakın ve eşit dağılımlı yapacak muhtemel iki farklı optimizasyon senaryosunu ileri sürdük. İlkinde kan basıncındaki değişim ile malzeme yapısında oluşan değişimler, ikincisinde ise aynı kan basıncı değişimine karşılık malzeme boyutlarında oluşan değişimler incelendi.

To my family and memory of my father

Acknowledgement

I would like to acknowledge my advisor, Dr. Kerem Pekkan for his precious support and assistance over the course of graduate studies. His sound knowledge and past research experiences about the biomechanics were valuable for me.

I would also like to thank Dr. Şenol Pişkin and Erhan Emek for their assistance during my thesis work. Likewise, all the members of Pekkan Laboratory were supportive during my research studies.

I would like to thank TUBITAK for scholarship provided.

Also, I would like to thank Graduate School of Science & Engineering, Koç University for their administrative and logistical support.

Table of Contents

List of Figures

List of Tables

Chapter 1 Introduction

Cardiovascular system is a major part of our circulatory system which is consisted of heart, arteries, veins and capillaries. Arteries are the main load carrying elements in this system since they are constantly subjected to higher pressures and flow compared to the veins. Systolic and diastolic (arterial) blood pressures in a normal adult are 120 mmHg and 80 mmHg, respectively. In pathological cases, the systolic blood pressure may increase even beyond 180 mmHg. In general, depending on ratio of their thickness to radius, arteries and veins are modeled as thick-walled or thin-walled axisymmetric cylindrical tubes in which principal stresses and wall shear stress are generated due to the internal blood movement (Figure 1.1). Soft tissues like arteries and veins are hyperelastic (time-independent material properties) materials where the principal Cauchy stress components are derived from strain energy density function that corresponds to the Helmholtz free energy.

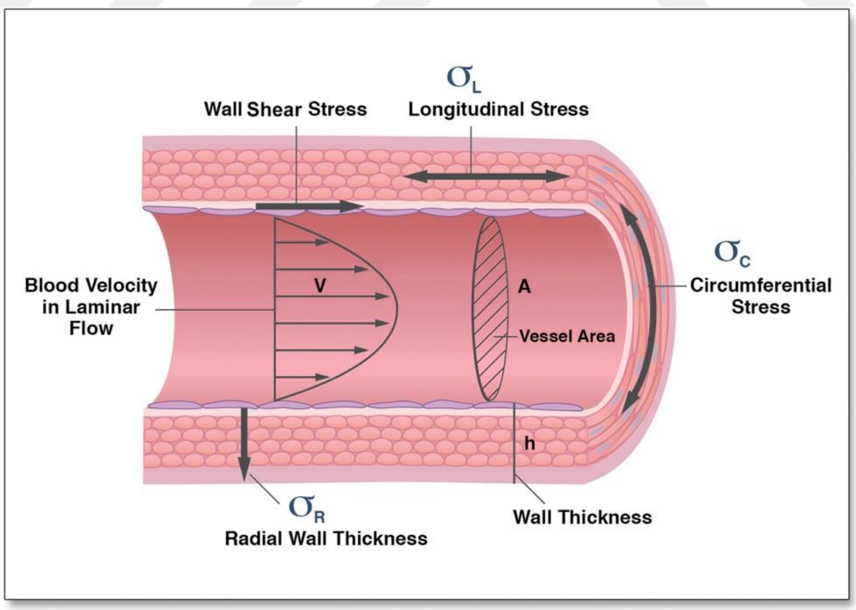

Figure 1.1: Major vascular cell types and the principal stress components of an arterial segment in cylindrical coordinates: circumferential stress σ_C, longitudinal stress σ_L, radial stress σ_R, and wall shear stress as well as blood velocity profile of Poiseuille flow [1].

1.1. Residual Stresses

Cardiovascular mechanics is a relatively recent field of biomechanics. Its emergence dates back to Y. C. Fung's earlier theoretical studies mechanical properties of soft tissues such as skin, lung and cardiovascular tissues around 1970s [2-7]. Patel and Vaishnav introduced polynomial strain energy density function for the aortic tissue, which has been considered to be incompressible and curvilinearly orthotropic [8]. Later, Fung et al. formulated the pseudo strain energy function for arteries expressed in an exponential form in two-dimensions (2D) [9]. In the same study, they performed inflation and axial stretch experiments on rabbit arteries in order to determine the corresponding material parameters appearing in their exponential strain energy formulation. They generalized their pseudo strain energy function into three-dimensions (3D) [10]. These approaches become extremely important for the patient-specific finite element modeling tools that become widely available during the last decade. The existence of residual stresses introducing a new hypothetical description of formation of residual stresses in arteries are also included [11]. In Fung's model, opened-up stress-free configuration is taken to be the reference state for arteries. In this state, arc shaped geometry has an opening angle, inner and outer radii, which define the level of deformation to close up the open sector. Residual stresses occur in unloaded tube after applying the bending to close the open sector. It is obvious that the presence of residual stress affects the total stress distribution generated in loaded states. Takamizawa and Hayashi also proposed a different approach to reveal the existence of residual stresses [12]. They used logarithmic strain energy density function in order to estimate the stress distribution through the wall thickness of the canine carotid artery based upon the assumption of constant circumferential strain. Delfino et al. constructed 3D finite element model of the carotid artery bifurcation to compare the stress field with and without residual stresses using the exponential strain energy function [13]. Later, Rachev and Greenwald reviewed existing experimental methods for measuring residual strains and how opening angle changes with arterial position, age, smooth muscle activity, mechanical environment and specific vascular pathologies [14]. In 2000, Holzapfel, Gasser and Ogden developed a new constitutive model for the passive mechanical response of arterial tissue [15]. In this model, the artery is considered to be two-layered orthotropic thick-walled nonlinearly elastic cylindrical tube. Two layers media and adventitia consist of two families of collagen fibers in symmetrical helices. They examined the mechanical response of an artery subjected to the combination of loadings such as inflation, axial extension and torsion to determine three material parameters for each layer. They also examined the effect of residual stresses on the stress distribution in the physiological state. Afterwards, Donmazov et al. introduced a new approach to estimate residual strains and stresses together with material parameters using noninvasive measurement techniques [16], as described in the present thesis. Application of this approach is further validated on a finite element model of a general two-layered artery, where the material remodeling and residual strain generation are investigated.

1.2 Tensile Tests and Buckling Studies

In addition to the inflation, axial extension and torsion tests, uniaxial and planar biaxial tensile tests are also common methods of determining linear and nonlinear material properties of soft tissues. Synthetic materials used as surgical vascular conduits may be stiffer than soft tissues. For these kinds of materials biaxial tensile tests are more viable than others. Bernal et al. developed a different technique to examine the linear isotropic material properties of soft tubes and pig carotid arteries using sonometry [17]. Piezoelectric crystals are used to track strains in the circumferential and longitudinal directions occurring due to the inflation of tubes and blood vessels. Furthermore, Zeinali-Davarani et al. examined the change in mechanical response of elastase-treated porcine aortic tissue at different stages of digestion using exponential strain energy function [18]. They showed that collagen fibers become active at small deformations under biaxial tensile loadings when the major part of elastin is degraded in stress-free state.

Along with determining mechanical characteristics of surgical vascular conduits, tracking their mechanical behavior in time is another challenging issue in order to prevent post-surgical complications, such as vessel tortuosity and buckling. Vascular buckling is an undesirable mechanical phenomenon that could restrict blood flow, thus should be predicted before the surgical intervention. It occurs due to the alteration in mechanical properties and geometry of the native vessels and surgical elastic materials subjected to mechanical load. Hence it is essential to select the optimal material and geometry with appropriate dimension for the reconstruction of vascular conduits. Han et al. examined different forms of vascular buckling in arteries and veins using linear and nonlinear models [19-28]. They found that there is ambiguous relation between the critical buckling twist angle and lumen pressure. However they did not propose an exact analytic relation for this phenomenon. In this study, experiments demonstrated that the critical buckling twist angle increases linearly as the lumen pressure increases for different materials. Accordingly, we proposed a basic and useful mathematical tool to estimate the critical buckling twist angle using linear elastic material properties such as Young's modulus and Poisson's ratio in case the lumen pressure is zero. We also computed material parameters of the porcine pericardium and human pericardium using Fung's 2D pseudo strain energy function for comparison.

1.3. Vascular Growth and Remodeling Associated with Optimization

According to Beloussov's hyper-restoration (HR) hypothesis, deviations of stresses from homeostatic stresses result in growth [29]. In growing material, material properties are altered (remodeling) to preserve the compatibility condition, thus generating residual stresses. Therefore, vascular growth, remodeling and residual stresses are interrelated closely. Patrick et al. combined the theory for volumetric growth (Rodriguez et al., 1994) and the theory for matrix remodeling (Humphrey and Rajagopal, 2002) to analyze stress dependent growth, contractility of the muscle and turn-over of collagen fibers both for homeostatic conditions and for the temporal response to sudden hypertension [30]. Their model predicted the opening angle distribution through the length of the aorta with sufficient accuracy. They also tried to answer why aortic arches of some animals have relatively large opening angles (OAs) considering the fact OAs are related with growth and remodeling [31]. They used computational models to show that OAs mainly increase with the following factors: 1. Longitudinal curvature (torus model), 2. Elastin production during earlier development and 3. Loss in wall stiffness leading to the generation of residual stresses. Larry A. Taber used computational models to examine Beloussov's HR hypothesis, in which tissue actively responds to restore the perturbations in growth stresses by overshooting target stresses [32, 33]. He related the growth rate to the rate of stress overshoot being proportional to the difference between the current and target stresses. Results produced on models for stretching of epithelia, cylindrical bending of plates, invagination of cylindrical and spherical shells, and early amphibian development showed that morphogenesis is partly regulated by HR, even some of them entirely self-driven by HR once initiated by genetic factors.

Despite the fact that there are numerous effort put on examining the growth and remodeling of soft tissues very few done to relate them to the material and geometrical optimization. Again Taber introduced an optimization principle for the regulation of vascular morphology as an extension of Murray's law, which states that the diameter of the blood vessel is controlled by a mechanism that minimizes the total energy required to carry on the blood flow, sustain the blood volume and to promote smooth muscle tone [34]. He concluded that the optimal wall shear stress due to blood flow increases with the blood pressure. He also confirmed previous studies that the fluid shear stress in arteries is considerably large than it is in veins. Optimization method can be also applied to relate growth, remodeling and residual stresses to homeostatic stresses. In this study, we propose two vascular optimization scenarios. First, we tried to answer, how are the material properties remodeled (optimized) to minimize the root-mean square deviation of Cauchy stress components at new pressure state from the homeostatic (averaged) stress components at old pressure. Second, how residual strain parameters such as effective angle, inner and outer radii of the open sector of grown material and axial pre-stretched are optimized (increased) to minimize the root-mean-square deviation of Cauchy stress components at the growth state from homeostatic stress components at original state.

Chapter 2 Noninvasive In Vivo Determination of Residual Strains and Stresses

2.1. Introduction

Residual stresses play a central role in cardiovascular soft tissue mechanics as they influence the observed *in vivo* material response significantly and hypothesized to be an essential factor for the healthy physiology of the vascular lumen and matrix maintenance [35]. Residual stresses exist in both arteries and veins, even when all external loading is removed. They are generated due to deformations known as residual strains within the tissue wall associated with kinematic compatibility constrains as well as vascular growth and remodeling such as new matrix synthesis or smooth muscle activation.

Numerous studies emphasized the structural function of the residual strains [36, 37]. Particularly, residual strains poses a well-known ability to homogenize the stress distribution in the arterial wall thus optimizes the load bearing capability. In addition they can also make arteries more compliant by providing a nonlinear elastic nature to address with high pressure levels and exhibit more effective local control over the arterial diameter by means of smooth muscle cell activation [14]. Therefore residual stresses are essential for the physiological vascular control or can act as a structural optimization agent that can be preferred over vascular remodeling, which requires more expensive matrix synthesis.

While there exist a variety of non-invasive techniques to measure residual stresses that are amiable to industrial applications [38, 39], for biomedical applications residual stresses are measured through *in vitro* experiments of excised vessel specimens where geometric constraints are removed sequentially through invasive directional vessel cuts. This well-established experimental technique is pioneered by Chuong and Fung, who conducted *in vitro* experiments [9] and determined the residual strains in a rabbit thoracic artery at its *unloaded state* by measuring the effective angle, inner radius and outer radius in zero-stress configuration and inner radius in unloaded state [40]. Another approach, proposed by Takamizawa and Hayashi, was that circumferential strain is assumed to be constant through the dog carotid artery arterial wall cross-section under physiological loading condition, so that the computed circumferential stress distribution was almost uniform [41]. Through this assumption the existence of residual strains and stresses within the wall became evident. Several subsequent investigations confirmed the existence of residual strains in different arteries, besides in other cylindrically shaped soft tissues such as the left ventricle [42-44], veins [45, 46], trachea [47], brain [48] and embryonic ventricle [49]. Thus far, no one considered the significance of the axial pre-stretch. Later, Alford et al. [50] showed that arteries with delayed elastin production grow longer than arteries in which elastin is produced early in development and in the presence of axial growth, the stretch has no effect on the opening angle (i.e. effective angle). In contrast, if axial growth does not occur, then the opening angle depends strongly on the *in vivo* axial pre-stretch. Soon after, Wang et al. described the use of longitudinal opening angle, since based on their conclusion the radial cut of the arterial ring segment cannot describe the zero-stress reference configuration of arteries [51].

The material properties of vascular soft tissues remodel *in vivo* due to physiological, genetic, mechanical and environmental factors [52]. For example, embryonic tissue becomes less compliant with age due to collagen synthesis. Likewise smoking and high blood pressure makes blood vessels to become stiffer but at a different timescale. While it is not straightforward to differentiate residual stresses from material properties it is hypothesized that residual stresses should also change dramatically during vascular remodeling and embryonic vascular growth, similar to the material properties. To extract this important parameter, a noninvasive experimental methodology is developed to track and quantify the *in vivo* residual stress levels in the vascular tissue. Therefore in this manuscript we present an analytical approach to estimate the vascular residual stresses *in vivo* at cylindrical vessels through non-invasive measurements of pressure and vessel geometry.

The present chapter is organized as follows; in the Methodology section, constitutional relations, numerical approximation, finite element model and various test cases are presented, followed by the key aspects of the present computational algorithm. In the Results section, first the effects of increase in experimental data points, addition of Gaussian noise to the data set obtained from the diastolic-systolic pressure range and choice of different strain energy function are examined for *in vitro* validation of material parameters and residual strain parameters and the residual stress distribution computed for each artery is compared with corresponding the result based on *in vitro* tests. In the second part, material parameters, residual strain parameters and corresponding residual stress distribution are computed for swine iliac artery based on *in vivo* experimental data. In the Discussion section, we analyze the predictive capability and limitations of present mathematical approach by discussing computed results and its possible future application on the embryonic chick vessel. In the Conclusion section, we also discuss the advantages of present *noninvasive* technique on the prediction of pediatric vessel growth over *invasive* classical experimental methods.

2.2. Methods

A general formulation is proposed to determine the effective angle and the effective radii in stress-free state, unloaded inner radius and *in vivo* axial pre-stretch in order to estimate residual strains and stresses from standard *non-invasive* measurement techniques. This approach also allowed the prediction of vascular material properties with reasonable accuracy. For brevity, the methodology is illustrated here using the stain energy formulation but it can be easily formulated for more complex multi-structural material models [15, 53, 54].

2.2.1. Representation of the Vascular Loading States

In Figure 2.1, 3D axisymmetric vessel wall is presented at its key loading states. The vascular lumen is treated as a cylindrical tube assuming that it has homogeneous material properties through the wall and it is cylindrically orthotropic. Another assumption is that the vessel wall should become an open sector with constant curvature after removing residual stresses from unloaded state$^{(0)}$. We also assumed that the vessel length does not change during the transformation from stress-free state to unloaded state$^{(0)}$. Additionally, the axial pre-stretch is taken into account while transforming the unloaded state$^{(0)}$ into unloaded state$^{(1)}$. Subsequent loaded states are defined as state 2, 3, … ,N. Coordinates of material points in described states are (R, Θ, Z), $(r^{(0)}, \theta^{(0)}, Z)$, $(r^{(1)}, \theta^{(0)}, z)$ and $(r^{(k)}, \theta^{(k)}, z)$ for $k=2,3, \ldots ,N$, respectively. Similarly, backward subsequent unloading states for $k=N,N-1, \ldots ,2$ are required to represent viscoelastic nature of soft tissues as the variation in mechanical and material properties due to the previous corresponding effects of loading states. Subscripts *i* and *o* denote the inner and outer wall radii at various states, Θ_0 represents half of the angle of open sector at stress the stress-free configuration.

In addition to the Fung's representation of states of artery [40], in the present formulation an intermediate unloaded state$^{(1)}$ is included. This new intermediate loading state corresponds to the case with zero intramural pressure, but with the *in vivo* axial pre-stretch. After cutting the vessel axially, it is shortened and its radii are changed. Finally, making radial cut releases all residual stresses and cylindrical tube becomes an open sector with the same length but with altered radii.

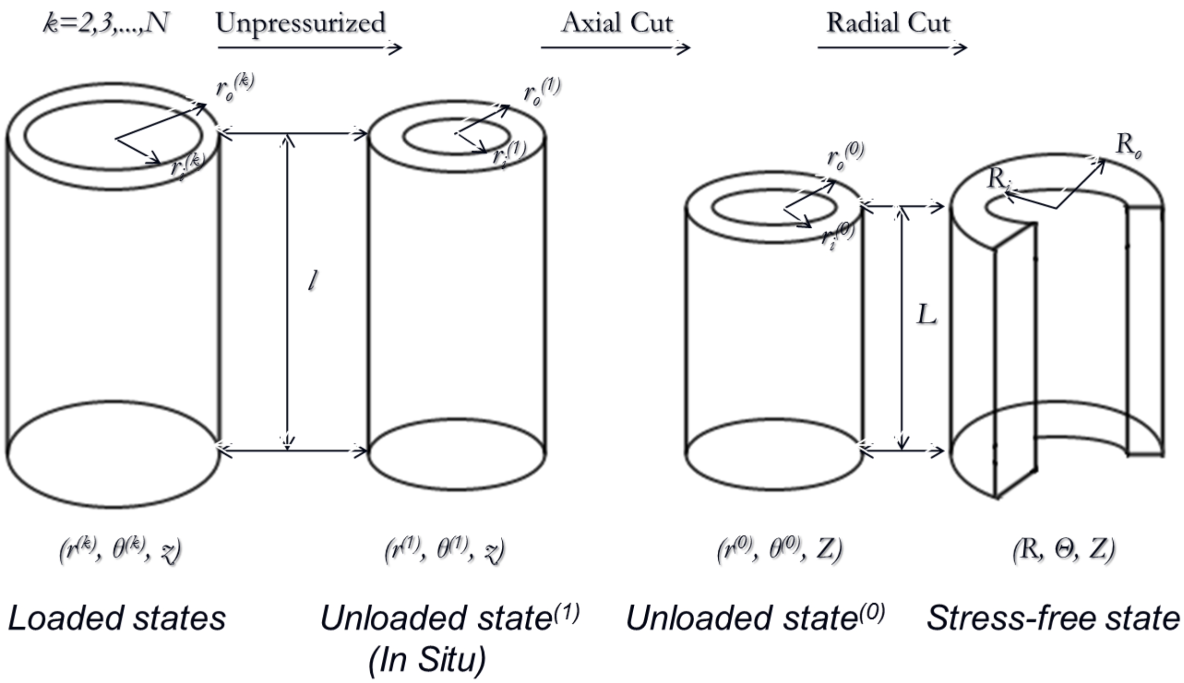

Figure 2.1: General geometrical representation of 3D vessel wall in zero-stress reference state, unloaded state$^{(0)}$, unloaded state$^{(1)}$ and subsequent loaded states under transmural pressure and axial forces.

2.2.2. Constitutive Relations

The finite theory of plane strain deformation leads the following description for the residual circumferential and radial stretch ratios for homogeneous and cylindrically orthotropic arterial wall [40];

$$\lambda_\theta = \frac{\pi r}{\Theta_0 R}, \quad \lambda_r = \frac{1}{\lambda_\theta \lambda_z}, \; \Theta_0 = \pi - \alpha \,,$$

$$r = \sqrt{r_i^2 + \frac{\Theta_0}{\pi}\left(R^2 - R_i^2\right)}, \tag{2.1}$$

where θ and α are the effective angle and the opening angle, respectively. r and R are the radii of an arbitrary point and r_i and R_i the inner radii in the unloaded and stress-free state, respectively. R_o is the outer radius in the stress-free configuration.

It is assumed that the deformation in the longitudinal direction occurs only during the transformation from unloaded state$^{(0)}$ into unloaded state$^{(1)}$, rather than from zero-stress state into unloaded state$^{(0)}$ does not occur, the corresponding residual Green strains are

$$E_\theta = \frac{1}{2}\left(\lambda_\theta^2 - 1\right),\ E_r = \frac{1}{2}\left(\lambda_r^2 - 1\right),\ \ E_z = \frac{1}{2}\left(\lambda_z^2 - 1\right), \tag{2.2}$$

In present manuscript we selected and tested two classical strain energy functions, Fung's exponential pseudo-strain energy function [10] and Delfino's exponential strain energy function [13], to verify and illustrate our mathematical approach.

Fung's exponential pseudo-strain energy function is given by

$$\rho_0 W = \frac{c}{2} e^Q$$

(2.3)

where

$$Q = b_1 E_\theta^2 + b_2 E_z^2 + b_3 E_r^2 + 2b_4 E_\theta E_z + 2b_5 E_z E_r + 2b_6 E_r E_\theta \tag{2.4}$$

Since the arterial wall is assumed to be an incompressible, strain energy function is modified by adding a Lagrangian multiplier to handle the incompressibility condition explicitly. This condition can be released if needed but kept here for simplicity. After defining the transformation from the reference state to the deformed state in terms of the coordinates X_α and x_i in the undeformed and deformed states, respectively, Cauchy stress components are obtained as

$$\sigma_{ij} = \frac{\rho}{\rho_0} \frac{\partial x_j}{\partial X_\alpha} \frac{\partial x_i}{\partial X_\beta} \frac{\partial}{\partial E_{\beta\alpha}} \rho_0 W^*,\ \left(i, j, \alpha, \beta = r, \theta, z\right) \tag{2.5}$$

where ρ, ρ_0 correspond to the densities of material in the deformed and undeformed states, respectively, and $\rho_0 W^*$ is he modified strain energy function.

For the Delfino's exponential strain energy function,

$$\bar{\Psi} = \frac{a}{b}\left\{\exp\left[\frac{b}{2}\left(\bar{I}_1 - 3\right) - 1\right]\right\}, \tag{2.6}$$

Cauchy stress tensor due to isochoric effect is given by

$$\bar{\sigma} = 2\bar{\Psi}_1 dev\bar{b} , \tag{2.7}$$

where $\bar{\Psi}_1 = \partial\bar{\Psi}/\partial\bar{I}_1$ and $\bar{b}$ is the modified left Cauchy-Green tensor and the operator and the operator $dev(\bullet)$ is defined by

$$dev(\bullet) = (\bullet) - \frac{1}{3}\left[(\bullet) : I\right] I , \tag{2.8}$$

Note that for nearly incompressible material $J \approx 1$.

Finally, the pressure integral equation is obtained substituting the circumferential and radial Cauchy stress components into the radial equilibrium equation, and integrating in terms of radii from the undeformed configuration:

$$p_i = \int_{R_i}^{R_o} c[(1+2E_\theta)(b_1 E_\theta + b_4 E_z + b_6 E_r)$$

$$-(1+2E_r)(b_6 E_\theta + b_5 E_z + b_3 E_r)]e^Q \frac{R}{R^2 - R_i^2 + \frac{180\lambda_z r_i^2}{\Theta_0}} dR, \tag{2.9}$$

Since the measurement of axial force requires *invasive* techniques, the axial force equilibrium is not taken into account explicitly.

2.2.3. Numerical Integration Framework

Gauss quadrature formula for a general case is given by

$$\int_a^b f(x)dx \approx \frac{b-a}{2}\sum_{i=1}^{n} w_i f\left(\frac{b-a}{2}x_i + \frac{a+b}{2}\right), \tag{2.10}$$

where a and b are the lower and upper bounds of the integral, respectively, n is the number of (nodes) the roots and x_i is the i^{th} root of the n^{th} order Legendre polynomials; its weight w_i is given by

$$w_i = \frac{2}{\left(1-x_i^2\right)\left[P_n'\left(x_i\right)\right]^2}, \tag{2.11}$$

For present problem, radium equilibrium equation is written in its compact form, in terms of circumferential and radial stress components

$$p_i = \int_{R_i}^{R_o} \left(\sigma_\theta - \sigma_r\right)\frac{R}{R^2 - R_i^2 + 180\lambda_z r_i^2 / \Theta_0} dR, \tag{2.12}$$

Gaussian quadrature formula is given by

$$p_i \approx \sum_{j=0}^{5} w_i f\left(R_j\right)\frac{R_j}{R_j^2 - R_i^2 + 180\lambda_z r_i^2 / \Theta_0}, \tag{2.13}$$

Pressure integral function is discretized by using Gaussian Quadrature formula, where R_j are quadrature nodes and roots of 6$^{\text{th}}$ order Legendre polynomial $L_6(R) \in P_6$ in the interval *[Ri, Ro]* with degree of exactness “11”, which gives the exact solution for P_{11}.

Two separate models model are presented based on discretized pressure function Eq. (13) for each strain energy formulation. For Fung’s SEF, 10 parameters model (10 PM) is formulated in terms of 7 material parameters and 3 residual strain parameters, where *in vivo* axial pre-stretch is assumed to be known and 11 parameters model (11 PM) additionally includes the axial pre-stretch as an unknown. For Delfino's SEF, 5 parameters model (5 PM) in terms of 2 material parameters and 3 residual strain parameters and 6 parameters model (6 PM) including the axial pre-stretch are introduced.

2.2.4. Test Cases

This technique is first tested against *in vitro* experiments where residual stress is also measured invasively. Invasive residual stress measurements are compared with present analytical predictions. Pressure-inner radius curves obtained by Rachev and Holzapfel for rabbit thoracic artery [14], rabbit carotid artery and human carotid artery [15] are digitized to simulate experimental data sets with various sampling sizes. For instance, we sampled 10, (9+1), 11 (9+2), 17 and 33 data points from the pressure interval of 0-160 mmHg corresponding to the pressure increments of 20, 10 and 5 mmHg, respectively. 10 and 11 data points were considered as a minimum experimental data set conditions for 10 PM and 11 PM, respectively. In general, the non-invasive *in vivo* physiological measurements will be limited to the cardiac cycle loading conditions. To illustrate this effect, 16 experimental data points covering the diastolic-systolic pressure range (approximately 60-120 mmHg) are also utilized for the prosed residual stress prediction technique. In this study we applied our technique to three artery types, having significantly different material properties represented by two different strain energy formulations. In addition we studied the effect of experimental noise on residual stress estimates. Complete experimental validation matrix is provided in Table 2.1.

Beyond the *in vitro* validation, we used *in vivo* pressure – outer diameter experimental data set for swine iliac artery [55] to estimate residual strains and stresses based on Fung's SEF. To give an insight about *in vivo* measurement technique of obtaining relevant data sets, *in vivo* measurements were performed on eight swine iliac arteries and the mean of pressure – outer diameter data points was obtained, where the outer diameter of arteries were measured by using the periarterial dimensional clip-probe imaging technique during the physiological loading and unloading states, and intravascular measurements of pulsatile blood pressure were performed with a pressure transducer.

Table 2.1. Experimental data sets with known residual stress and material properties where the present analytical approach is tested. The effect of more resolved experimental data sets are simulated by increased experimental data points obtained through higher-order digitizing procedure. Likewise synthetic experimental error is included to verify the robustness of present approach. A large range of arterial material properties for rabbit carotid and thoracic artery as well as human carotid artery are tested subject to two different strain energy formulations. The effect of adding experimental noise to the same experimental data set from diastolic-systolic pressure region is also analyzed for each artery type.

Invasive Measurements	Pressure Range (mmHg)	Number of data points tested
Rabbit Carotid Artery Fung's SEF [21]	0 – 160	10, 11, 17, 33, 16
Rabbit Thoracic Artery Fung's SEF [14]	0 – 180	10, 11, 19, 37, 16
Human Carotid Artery Delfino's SEF [13]	0 – 200	11, 21, 41, 16

2.2.5. Notes on the Computational Algorithm

A standard nonlinear least-squares curve fitting is implemented for each experimental data set with the objective function of discretized pressure function, using the *trust-region-reflective algorithm* for constrained optimization problem. In order to guarantee the convergence to physical local minima, it is essential to choose an appropriate physical interval for each variable. For example, by its definition material parameters appearing in both strain energy functions must be positive real numbers, the effective angle Θ_0 is defined in the interval 0 – 180 degree, the axial pre-stretch λ_z is searched in the interval 1.0 – 2.0 and the effective radii are expected to be greater than the radii corresponding to the minimal *in vivo* pressure value of 60 mmHg for each *in vitro* case, 123 mmHg for swine iliac artery, and less than twice of these values.

2.2.6. Finite Element Model of Residual Stress Generation

The three-dimensional finite element model of a circular artery is developed using ADINA (ADINA R&D Inc, Watertown, MA) for further validation of the proposed formulation. The loading states in Figure 2.1, including material remodeling are simulated sequentially using wires to achieve vessel closure from stress-free states. Snapshots from this model are plotted in Figure 2.2 with boundary wire elements closing open ends to achieve residual stress generation in Figure 2.2 (ii). The artery geometry is specified as a thick-walled cylindrical tube subjected to external loading with 120 hexahedral elements as shown in Figure 2.2 (iv). Existence of compatibility conditions between each of the loading state is verified. The arterial wall is modeled as a two-layer (media and adventitia) incompressible hyperelastic fiber orientation model [9, 10]. Each layer of the artery is modeled as a cylindrical orthotropic fiber-reinforced composite. Layers are modeled with separate strain-energy function and the neo-Hookean model is used to determine the isotropic response of each layer. Material parameters and dimensions of geometry are obtained from rabbit carotid artery [9, 10].

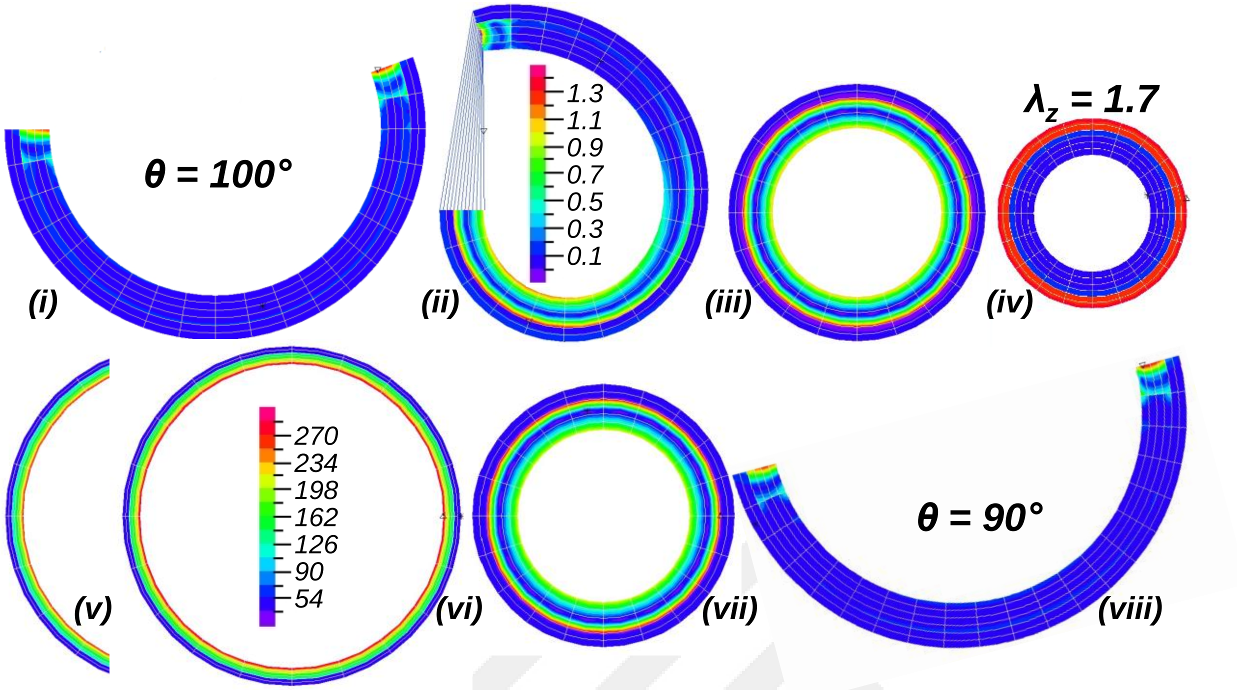

Figure 2.2: The two-layer micro-structure finite element model of residual stress generation. Series of vessel cross-sections representing (i) the Stress-Free open configuration of the baseline rabbit carotid artery having an effective angle of 100°**,** (ii) mid-vessel closure towards the fully-closed Unloaded State achieved by thrust elements pulling the open ends, (iii) Unloaded State$^{(0)}$, (iv) Unloaded State$^{(1)}$ with pre-stretch –only mesh shown and (v) the Loaded State$^{(2)}$ –section of vessel is shown Material properties are then altered representing the vascular remodeling by (vi) the remodeled Loaded State$^{(3)}$ and its corresponding (vii) remodeled unloaded configuration and (viii) remodeled stress-free state resulting an effective angle of 90**°**. Color and legends correspond to the magnitude of Cauchy stress distributions (mmHg). Legend in (vi) corresponds to vessel cross-sections in (v) and (vi), while legend in (ii) correspond to all other states.

2.3. Results

2.3.1. *In Vitro* Validation

A. Effect of Number of Experimental Data Points

The accuracy of estimated residual strain parameters and material parameters for each artery are tested by altering the number of experimental data points corresponding to the pressure increment of 20 mmHg, 10 mmHg and 5 mmHg. The response of alteration in number of unknown parameters is also analyzed by introducing 10 PM and 11 PM. Table 2.2 shows results for 10 PM with increasing number of experimental data points, 10 (9+1), 17 and 33 data points, for rabbit carotid artery, where the pressure interval is given as 0 – 160 mmHg. Although material parameters exhibit some level of deviations from results obtained based on *in vitro* experiments, due to their high sensitiveness regarding to the nonlinearity presented in Fung's SEF, the range of local error introduced in each material parameter is acceptable. Whereas the computed residual strain parameters corresponding to each experimental data set demonstrate better agreement. More particularly, the similar trend, relative error 0 – 3.4%, is preserved after addition of another unknown, the axial pre-stretch into the system (Table 2.3). In all cases, increase in number of experimental data points does not really affect the accuracy of results, but still causes slight improvement in values.

Table 2.2. Numerical values of 10 parameters model, where material parameters and residual strain parameters are computed using 10, 17 and 33 experimental data points for rabbit carotid artery compared with results based on *in vitro* experiments [15].

	Material Parameters							Residual Strain Parameters		
Number of data points	c (kPa)	b_1	b_2	b_3	b_4	b_5	b_6	Θ_0 (deg)	R_i (mm)	R_o (mm)
10	27.71	0.9942	0.4126	0.0089	0.0747	0.0227	0.0271	100.0	1.44	1.83
17	26.69	0.9922	0.4509	0.0004	0.0752	0.0181	0.0406	100.0	1.44	1.83
33	27.93	0.9935	0.4297	0.0029	0.0747	0.0280	0.0093	100.0	1.44	1.82
Ref.	**26.95**	**0.9925**	**0.4180**	**0.0089**	**0.0749**	**0.0295**	**0.0193**	**100.0**	**1.43**	**1.82**

Table 2.3. Numerical values of constants appearing in 11 parameters model, where material parameters and residual strain parameters are computed using 10, 17 and 33 experimental data points for rabbit carotid artery compared with results based on *in vitro* experiments [15].

Parameters	Material Parameters							Residual Strain			
Number of data points	c (kPa)	b_1	b_2	b_3	b_4	b_5	b_6	Θ_0 (deg)	R_i (mm)	R_o (mm)	λ_z
11	27.24	0.9972	0.4418	0.0088	0.0747	0.0202	0.0253	99.9	1.45	1.83	1.71
17	27.29	0.9925	0.4204	0.0000	0.0750	0.0178	0.0409	100.1	1.44	1.83	1.71
33	27.59	0.9938	0.4482	0.0043	0.0747	0.0283	0.0075	100.0	1.44	1.81	1.71
Ref.	**26.95**	**0.9925**	**0.4180**	**0.0089**	**0.0749**	**0.0295**	**0.0193**	**100.0**	**1.43**	**1.82**	**1.70**

B. Effect of Experimental Noise

The effect of experimental noise is analyzed by adding Gaussian noise to experimental data points obtained from diastolic-systolic pressure range for each artery in the order of 1 Pa for internal pressure and 0.01 mm for inner radius. These error ranges correspond to a typical servo-null micro pressure measurement. We also tested the effect of increased error ranges in the order of 1 mmHg (133.22 Pa) and 0.1 mm for internal pressure and inner radius, respectively, which correspond to a large artery cuff pressure measurement scenario. Table 2.4 demonstrates a good quantitative agreement in predicting *in vivo* residual strain parameters together with material parameters for rabbit thoracic artery based on the same strain energy formulation.

Table 2.4. Numerical values of constants appearing in 11 parameters model, where material parameters and residual strain parameters are computed using 16 experimental data points from the diastolic-systolic pressure range without (DS) and with the addition of Gaussian noise for rabbit thoracic artery in the order of 1 Pa and 0.01 mm (DSN1) and in the order of 1 mmHg and 0.1 mm (DSN2) [40].

	Material Parameters							Residual Strain Parameters			
Number of data points	c *(kPa)*	b_1	b_2	b_3	b_4	b_5	b_6	Θ_0 *(deg)*	R_i *(mm)*	R_o *(mm)*	λ_z
DS	21.85	1.0921	0.4750	0.0352	0.0921	0.2270	0.0000	71.4	3.93	4.67	1.691
DSN1	24.30	1.0613	0.3791	0.0593	0.0890	0.0000	0.0496	71.4	3.92	4.53	1.691
DSN2	23.41	1.0697	0.4099	0.1207	0.0778	0.0002	0.0346	71.4	3.92	4.54	1.691
Ref.	**22.40**	**1.0672**	**0.4775**	**0.0499**	**0.0903**	**0.0585**	**0.0042**	**71.4**	**3.92**	**4.52**	**1.691**

C. Parameters of Delfino's SEF

Computed material parameters a and b, and residual strain parameters the effective angle Θ_0, the effective radii R_i and R_o, and *in vivo* axial pre-stretch λ_z are presented in Table 2.5. Results show that choice of appropriate strain energy formulation has an impact on the estimation of parameters. Delfino's formulation leads to greater local errors (0.6 – 7.5%) in each parameter.

Table 2.5. Numerical values of constants appearing in 6 parameters model, where material parameters and residual strain parameters are computed using 11, 21, 41 experimental data points and 16 experimental data points from the diastolic-systolic pressure range without (DS) and with the addition of Gaussian noise for human carotid artery based on Delfino's SEF (DSN) [15].

	Material Parameters		Residual Strain Parameters			
Number of Data Points	a *(kPa)*	b	Θ_0 *(deg)*	R_i *(mm)*	R_o *(mm)*	λ_z
11	38.72	18.13	127.1	4.58	5.76	1.08
21	47.15	16.44	130.0	4.43	5.33	1.08
41	39.85	17.58	135.4	4.27	5.40	1.08
DS	40.88	17.04	128.3	4.56	5.46	1.12
DSN	38.67	17.27	126.8	4.65	5.58	1.13
Ref.	**44.20**	**16.70**	**130.0**	**4.46**	**5.36**	**1.10**

D. Computation of Inner Radius in Unloaded States

In order to determine residual strains defined as a transformation from stress-free state into unloaded state$^{(0)}$, unloaded state$^{(1)}$ and so on, additional parameters inner radii in both unloaded states are computed for each artery by using extrapolation after determining all parameters. Table 2.6 shows that results are consistent with experimental ones.

Table 2.6. Numerical values of inner radii in unloaded state$^{(0)}$ and unloaded state$^{(1)}$ compared with results based on *in vitro* experimental results for rabbit carotid artery [15], rabbit thoracic artery [40] and human carotid artery [15].

	Unloaded State$^{(0)}$ (*In Situ*)		Unloaded State$^{(1)}$	
Inner Radius, r_i (mm)	Experimental	Computed	Experimental	Computed
Rabbit Carotid Artery	0.74	0.73	0.71	0.71
Rabbit Thoracic Artery	1.38	1.35	1.35	1.37
Human Carotid Artery	2.96	2.96	3.10	3.15

E. Residual Stress Distribution

Residual stress distributions in both unloaded states are plotted for all three arteries (Fig. 2.3, Fig. 2.4 and Fig. 2.5). It can be deduced that the presence of axial pre-stretch in unloaded state$^{(1)}$ alters the residual stress distribution significantly and resulting in greater global error. Especially, for human carotid artery, estimated residual stresses significantly differ from its pairs obtained based on *in vitro* testing.

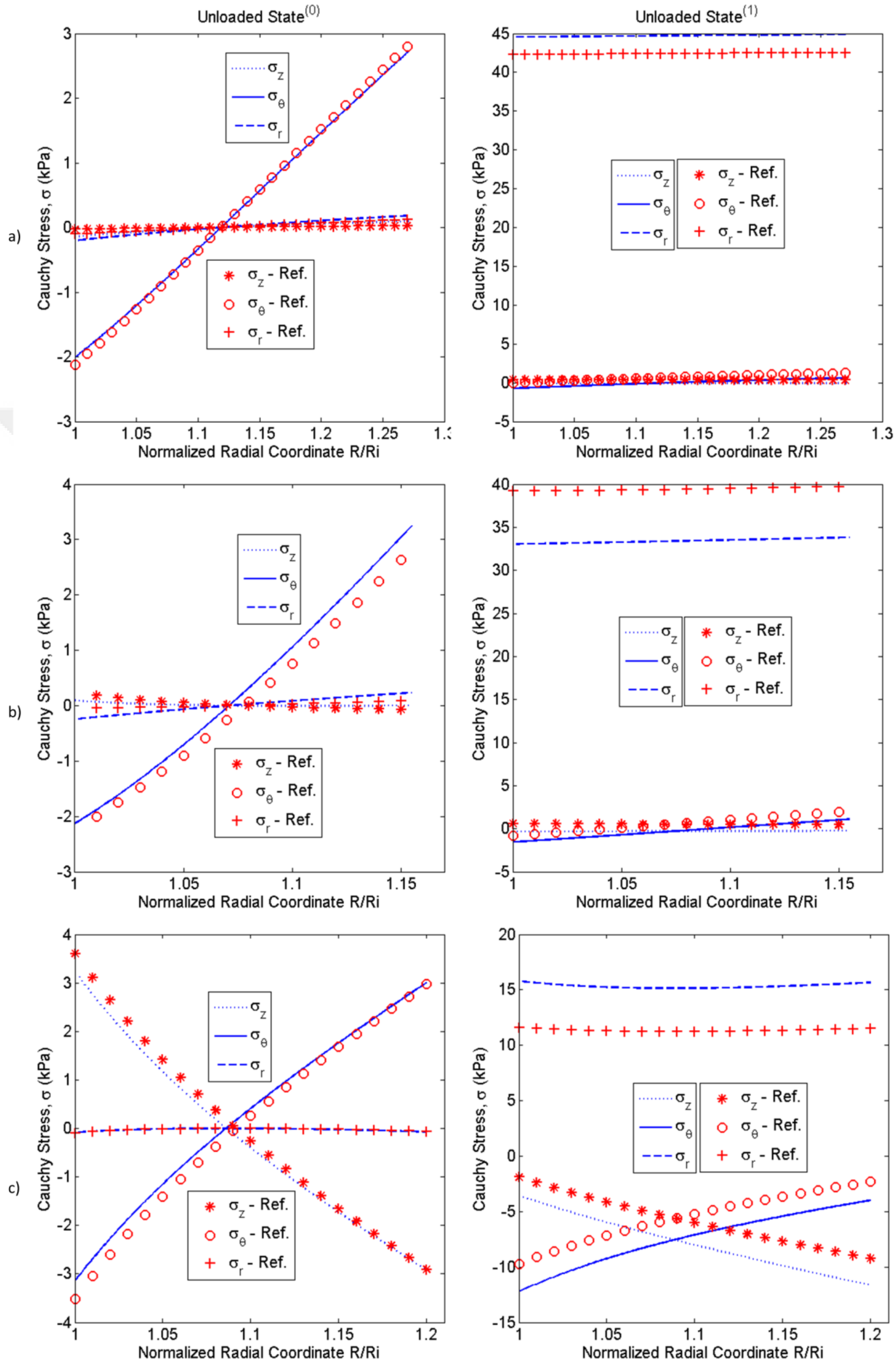

Figure 2.3: Residual stress distribution through the arterial wall in unloaded state$^{(0)}$ and unloaded state$^{(1)}$ in a) rabbit carotid artery, b) rabbit thoracic and c) human carotid artery, respectively, compared with experimental results (Ref.) based on *in vitro* data a) [15], b) [14] and c) [15].

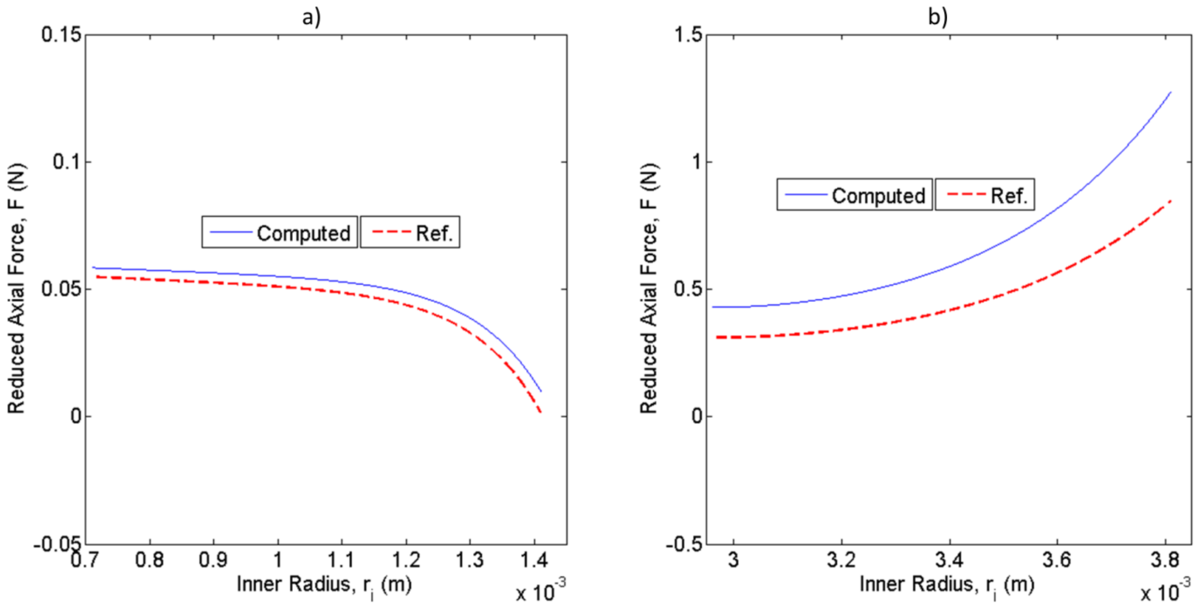

Figure 2.4: Axial force distribution through the arterial wall in a) rabbit carotid artery and b) human carotid artery compared with results (Ref.) based on *in vitro* experiments [15].

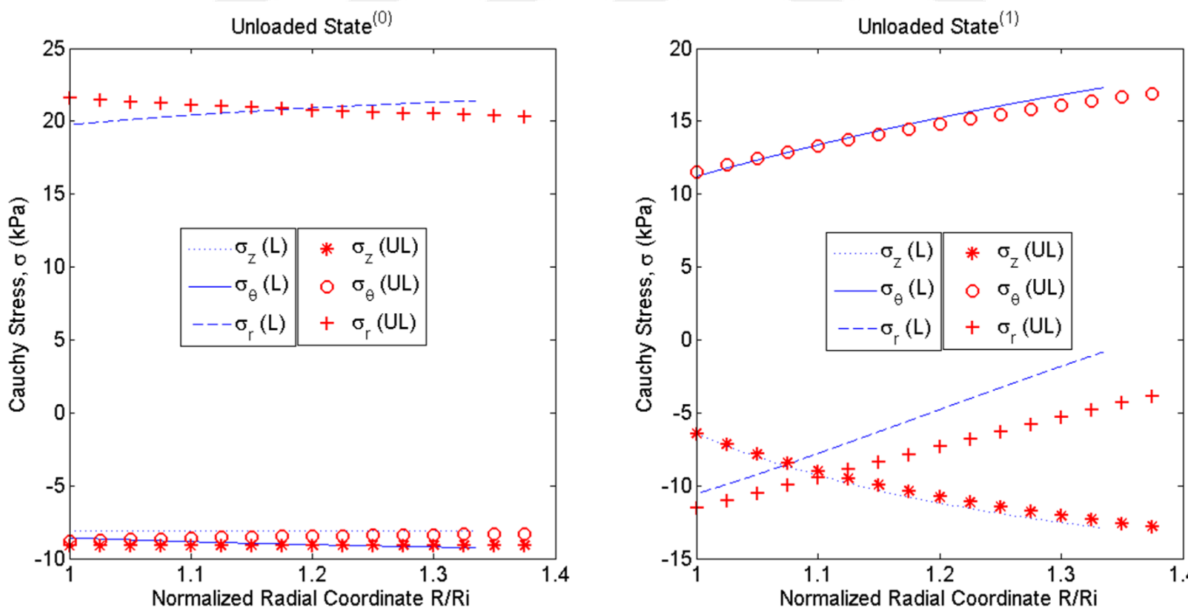

Figure 2.5: Residual stress distribution through the arterial wall in unloaded state$^{(0)}$ and unloaded state$^{(1)}$ in swine iliac artery during the loading (L) and unloading (UL).

F. Axial Force Equilibrium

Axial force distribution through the arterial wall is plotted to check the validity of disregarding the axial force balance, since the measurement of axial force requires *in vitro* interventions. In Fig. 2.4, reduced axial force is computed for rabbit carotid artery and human carotid artery using Fung's SEF and Delfino's SEF. Although both plots are consistent with results obtained based on *in vitro* measurements, resulting global error for human carotid is greater because of high sensitive structure of Delfino's strain energy function.

2.3.2. *In Vivo* Results

A. Nonlinear Regression and Parameter Estimation

Nonlinear least-squares curve fitting analysis is performed on experimental data sets, which were obtained from physiological state of swine iliac artery by using *in vivo* measurement techniques. Table 2.7 shows computed results for material parameters and residual strain parameters of swine iliac artery in loading and unloading states. Except *in vivo* axial pre-stretch, all other parameters demonstrate slight variations as expected. Increase in the material parameter c (kPa) indicates the stiffening of the arterial wall after subsequent loading steps.

Table 2.7. Numerical values of constants appearing in 11 parameters model, where material parameters and residual strain parameters are computed using experimental data points from the physiological state of swine iliac artery in loading and unloading states, respectively.

	Material Parameters							Residual Strain Parameters			
States	c *(kPa)*	b_1	b_2	b_3	b_4	b_5	b_6	Θ_0 *(deg)*	R_i *(mm)*	R_o *(mm)*	λ_z
Loading	16.08	0.0198	0.0645	7.2365	4.9803	0.8747	1.9429	110.1	2.60	3.47	1.22
Unloading	16.93	0.0000	0.0000	7.3053	4.9788	0.7731	1.8210	121.9	2.61	3.64	1.22

B. Residual Stress Distribution in Loading and Unloading States

Inner radii of swine iliac artery in unloaded state$^{(0)}$ and unloaded state$^{(1)}$ are extrapolated at zero pressure using the pressure – outer radius relation curves, where the inner radii in unloaded state$^{(0)}$ and unloaded state$^{(1)}$ were computed as 2.63 mm, 1.91 mm for loading states and 3.06 mm, 2.20 mm for unloading states, respectively.

Residual stresses are estimated in each unloaded state by using computed material parameters, residual strain parameters and inner radius of relevant state. Since soft tissues demonstrate a viscoelastic mechanical response, residual stress distribution in loading states and unloading states treated separately. Fig. 2.7 illustrates residual stresses for loading states and unloading states in the same plot without and with taking the existence of in vivo axial pre-stretch within the swine iliac artery into account.

2.3.3. Remodeled States and Validation with Finite Element Model

The finite element model allowed the generation of several synthetic experimental data sets for validation purposes. To illustrate the utilization of the present technique in a realistic growth and remodeling scenario we simulated a remodeled artery from its baseline material properties. Our baseline model corresponds to the Fung's artery model [9, 10] having an effective opening angle of 100 degrees. This artery is closed from its stress-free state where residual stress are generated and extended in the axial direction. Next the artery is inflated with the specified intramural pressure levels. The resulting pressure-inner radius data is extracted from the finite element model and used in our optimization formulation as an input. Accurate agreement with the specified opening angle in the finite element model vs. the present analytical approach is observed.

At this loaded baseline state the material properties are altered which corresponds to a remodeled artery *in slico*. Baseline material properties are provided in Table 2.8. Then, the artery is de-inflated to zero pressure state and shortened to closure state. It is then cut again to obtain the effective angle at zero-stress state. The effective angle after remodeling is computed to be 90 degrees. The pressure-radius data for the remodeled case is also used in our formulation and the remodeled effective angle is also computed accurately. In addition, the inner and outer radii were estimated for both cases, which were found within 10% vicinity. The results of these simulations are tabulated in Table 2.8. Stress distribution and geometry at several loading states, including baseline and remodeled cases are presented in Figure 2.2.

Table 2.8. Numerical values of constants appearing in 11 parameters model, where material parameters and residual strain parameters are predicted both for *baseline* and *remodeled* rabbit carotid artery using data points (pressure and diameter) obtained from the finite element model (FEM).

	Material Parameters							Residual Strain			
Material property	c (kPa)	b_1	b_2	b_3	b_4	b_5	b_6	Θ_0 (deg)	R_i (mm)	R_o (mm)	λ_z
Baseline	22.59	0.0529	0.0039	0.0284	0.0082	0.0000	0.0181	101.8	1.73	1.86	1.60
Remodeled	28.18	4.3329	0.3217	0.4987	0.9352	0.0358	0.6474	89.8.1	1.89	1.94	1.66
Baseline (FEM)	**26.95**	**0.9925**	**0.4180**	**0.0089**	**0.0749**	**0.0295**	**0.0193**	**100.0**	**1.43**	**1.82**	**1.70**
Remodeled (FEM)	**-**	**-**	**-**	**-**	**-**	**-**	**-**	**90.0**	**1.61**	**2.00**	**1.70**

2.4 Discussion

Arterial and venous vessel growth is known to be associated with the level of residual stresses. The rate of growth is hypothesized to depend on the difference between the present stress level occurring due to the external loading and the homeostatic stresses, according to the Beloussov's Hyper-restoration (HR) hypothesis [29]. HR hypothesis have not been fully validated through *in vivo* measurements due to the invasive nature of residual stress measurement techniques. Besides these experimental challenges, several studies indicate that residual stresses emerge as a result of elastic deformations occurring to ensure the compatibility of the growing tissue [56]. Thus, as a part of the total stress distribution, residual stresses play a significant role in the physiological and pathological growth process of the vascular system, while they arise due to the growth itself. This makes residual stresses and the growth and remodeling mutually interdependent. That is to say, knowledge of residual stresses can allow the prediction of vessel growth. This is particularly important for pediatric and fetal cardiac diseases and in their surgical repairs since vascular growth should be incorporated in the therapy or surgical intervention design [57, 58].

During the growth of vascular system the alteration in material properties (remodeling) is present while the tissue tries to make ongoing deformations compatible, so that residual strains and stresses are generated. Nevertheless, the fundamental mechanism driving the vascular growth and remodeling is not completely understood [33]. It is also widely accepted that the level of local residual stresses induces growth according to the HR hypothesis as a result of deviation in local stresses due to external loadings from the homeostatic stress state and *noninvasive* techniques are required to track the residual stresses in time. Therefore this paper focused on two aspects; first is the validation of the mathematical approach of computing residual strain parameters together with material parameters and corresponding residual strain and stresses with *in vitro* testing results, and the other is to estimate residual strains and stresses using experimental data sets obtained from *in vivo* measurement techniques.

The different features of the developed theoretical model influence its special numerical treatment. Naturally, ignoring the physical constraint in the axial direction may cause the loss of information about the nonlinear system, where it is compensated by proper selection of constraints for each of the unknown parameters that guaranties the convergence to the physical local minima, though there are several local minima arising from the nonconvexity of present strain energy function systems. The elegant way of describing the search interval for each unknown is to consider material parameters as a positive real numbers $(0, Inf)$, the effective angle Θ_0 in the interval $(0^0, 180^0)$, the axial pre-stretch λ_z in the interval $(1.0, 2.0)$ and the effective radii R_i and R_o in the interval $(r_i^{(LDP)}, 2\, r_i^{(LDP)})$ and $(r_o^{(LDP)}, 2\, r_o^{(LDP)})$, where $r_i^{(LDP)}$ and $r_o^{(LDP)}$ are the inner radius and outer radius in the lowest value of diastolic pressure, respectively. Another important point is the selection of initial estimates for each unknown, where each initial estimate is selected arbitrarily in defined intervals. After the first iteration, the computed parameters are used as the initial estimates for the second iteration in order to improve the accuracy of computed parameters.

One of the main goals of the present study was to validate proposed mathematical technique by performing subsequent computations in various realistic scenarios. It can be pointed out that computed results are strongly independent from the number of experimental data points and addition of Gaussian noise to the same data sets exhibiting well qualitative agreement with their *in vitro* counterparts (Table 2.2 – 2.5). Fig. 2.3 – 2.5 demonstrates adequate fit of the computed residual stresses with residual stresses plotted based on parameters obtained from *in vitro* measurements.

In the case of *in vivo* estimation of residual strains and stresses, associated parameters and stress distribution slightly differ for the loading and unloading states, while computed *in vivo* axial pre-stretch values were the same (Table 2.7). These variations present a novel message about the viscoelastic mechanical response of soft tissues demonstrating the pressure dependent remodeling in two subsequent loading and unloading states occurring during one cardiac cycle.

For highly curved vessels and three-dimensional patient specific arteries and veins a similar analytical formulation can be derived that includes the vessel curvature. While it may also feasible to partition the cylindrical vascular tube into several circular rings each having a finite thickness. This partitioned model can be analyzed based on a finite element formulation, and residual strain parameters and material parameters can be computed for each of the ring domain using the corresponding segmental experimental pressure-radius (diameter) data points obtained through *in vivo* measurement techniques.

In conclusion, it is merely sufficient to have knowledge of *in vivo* pressure-radius (diameter) relation in order to estimate residual strains and stresses in the vascular system. Therewithal, it should be emphasized that kinematic formulations presented in this study are based on assumptions of incompressible, homogeneous and cylindrically orthotropic vessel wall, and constitutive relations do not take into account the mechanical response of each micro-structure elements such as collagen, elastin and smooth muscle fibers considering the hyperelastic behavior of whole vascular tissue. However, the proposed mathematical technique does not restrict the choice of strain energy formulation (as in our finite element model that includes vessel constituents); contrariwise micro-structure models will introduce physical meanings of material parameters such as density and orientation of fibers and other complexities.

While the pulsatile pressure data can be obtained routinely through cardiac catheterization procedure for the specific vessel, the non-invasive pressure measurement techniques are also advancing and becoming available in clinics as an alternative. For example the patient specific pressure pulse wave can be acquired continuously [59, 60] including the pulse-oximetry devices correlating with the pressure waveform or through MRI [61]. Although these techniques are still in development phase, there are several encouraging results acquired with them [62-65]. Our proposed methodology can be integrated with these measurement modalities. Non-invasive techniques generally need a calibration step to estimate the pressure at the specific arterial vessel. One calibration approach is based on the auscultator method, which measures absolute Systolic Blood Pressure (SBP) and Diastolic Blood Pressure (DBP) noninvasively. The vessel radii can also be calculated noninvasively through ultrasound monitoring. Both flow and pressure data can be gated with ECG and thus synchronized. We applied this approach to study synchronized flow/pressure waveforms in congenital heart patients [66]. In summary, clinical data required for our methodology is available with today's techniques [33]. In the future, we will implement this validated technique to the experimental data set acquired in our laboratory using simultaneous optical coherence tomography [67] and servo-null pressure measurements of chick embryonic vessels, particularly embryonic great arteries [68]. This will provide the time-resolved growth rate of embryonic vessels and relate with the stress-dependent finite growth models. Another important application is the *in vitro* testing of small-sized vessels, which can be used to validate the present theoretical results further.

Chapter 3 Mechanical Characterization and Torsional Buckling Effects of Vascular Conduits

3.1. Introduction

Degenerative cardiovascular diseases result in a gradual loss of function through an efficient pathway until total failure , which will prevent the blood flow to the corresponding organs, or generate stroke. Those critical diseases include congenital heart diseases (CHD), heart failure and vascular diseases of aorta or pulmonary systems in adults. CHD diseases can feature an atrial or ventricle septal defects (ASD and VSD), missing heart walls, pulmonary atresia and aortic coarctation. In addition, adults have aortic aneurysms, which may rupture abruptly due to mechanical failure if not repaired in a timely manner. Surgical repair of cardiovascular diseases require reconstructive surgeries artificial conduits or patches are anastomosed to the native tissue of the failed heart or vascular region. For example, in a Fontan operation an artificial baffle type conduit is used to connect inferior vena cava (IVC) to the right pulmonary artery (RPA). As such neonatal cardiovascular operations involves an artificial shunt to direct flow from the ventricle or aorta to the main pulmonary artery (MPA). In these operations the xenograft bovine pericardium or artificial Dacron or Gore-Tex is used to patch and thus repair pulmonary artery atresia, aortic arch hypoplasia or ASV and VSD diseases.

As in native vessels the cardiovascular surgical conduits are subject to the physiological in vivo conditions that generate pulsatile flow and 3D cyclic loading. The suture lines of these materials also cause additional stress concentrations. Thus, surgical conduits should be structurally stable for a long time, biologically compatible and replicate the mechanical characteristics of the native cardiovascular tissue as close as possible. Also they need to sustain both the resting and exercise conditions of the patient.

Detailed analysis of the mechanical behavior of artificial baffle conduit and native tissue under mechanical loading is crucial to for the design of complex cardiovascular operations and can optimize the patient outcomes. Furthermore, mechanical testing and the knowledge in the baseline material properties are important for designing new cardiovascular materials that would over perform the existing technology. Thus in literature there exists numerous studies which investigate the mechanical responses of cardiovascular tissues and medical conduits. One of the very first studies was performed by Roy [69] and investigated the elastic properties of the arterial wall experimentally. Especially the vascular tissue has been investigated in detail, particularly by Chuong and Fung [70, 71] and his successors such as Holzapfel, Gasser, Ogden [15] and Humphrey [72] since 1984's. In this regard, a number of constitutive relations describing the mechanical response in this kind of tissue have been proposed [73]. For instant, the transmural stress distribution that strongly influences the mechanobiological processes occurring in the vascular tissue may be computed [72]. Due to its suitability in computational biomechanical modeling, the strain energy density function definition is preferred to describe and reproduce complex mechanical response of the vascular tissue [15, 73, 74]. For example, it is applied to study the mechanics of ageing of the human aorta [75].

The material characteristics of defected or diseased vascular tissue have also been investigated with this approach. Roy [69] has first found that a striking decrease occurs in the longitudinal elasticity in the aorta walls of advanced aged man and woman. In addition, the relation of the inner pressure to the aorta volume, i.e. distensibility, for diseased aortas, is quite different from healthy aorta. Garcia-Herrera et al [76] has modelled the in vivo mechanical response of the ascending aortic aneurysm in the Marfan syndrome using uniaxial testing. The region affected with the disease has an increased stress level compared to the unaffected part of the aortic arch. Sommer et al [77] investigated the strength of aneurysmatic and dissected human thoracic aortas via triaxial shear and uniaxial tensile testing. In total, 16 human thoracic aortas were investigated from which was found that the aortic media has much stronger resistance to rupture under 'out-of-plane' than the 'in-plane' shear loadings. Also, subject to different shear loadings the aortic tissues revealed anisotropic failure properties with higher ultimate shear stresses in the longitudinal than in the circumferential direction. Vande geest et al. developed a statistical model to noninvasively estimate the distribution of wall strength distribution in aortic aneurysms from the tensile testing of surgically procured abdominal aortic aneurysm wall specimens [78]. Monson et al [79] have studied the multi axial behavior of cerebral vessels. They have obtained twelve arteries from the surface of the temporal lobe of the patients undergoing surgery and subjected to various combinations of axial stretch and pressure around typical physiological conditions before being stretched to failure. In addition, they have compared axial and circumferential responses, and fit the measured data to a four parameter, Fung-type hyperelastic constitutive model. Mechanical characteristics of the artery were found to be nonlinear and anisotropic, with considerably greater resistance to deformation in the axial direction than around the circumference.

Different vascular diseases require conduits with different material properties. In addition, the compliance of the arteries that will be repaired or reconstructed does also matter on selecting the conduit material. Studies on biomedical material suggested several types of conduit materials that exhibit the physiological requirements. However, it is crucial to examine the material characteristics of these conduits before using in complex surgeries in a patient-specific manner. The biomedical conduits have been traditionally investigated under uni-axial and bi-axial loading. The patency of vascular grafts is associated with anastomotic intimal hyperplasia and thrombus formation. Especially the compliance mismatch between the graft and host artery result in differential mechanical strain and can augment intimal thickening [80]. The earliest studies on experimental mechanical testing of biomedical conduits goes back to 1979 [81]. Stress strain curves and relaxation curves of knitted and woven grafts of both Dacron and Teflon have been examined using a tensile testing instrument, and compared with those of the canine aortic arteries. The short term durability of the conduits are evaluated with respect to the material, type of weave, circular crimps and cut-out directions and found out that the viscoelastic properties largely depend on the material, not other features of the conduit. As such, Lucereau et al. [82] investigated the relation between the tensile tests and vascular compliance in polyester textile vascular prostheses. Three different models of commercially available knitted vascular prosthesis were studied using longitudinal and circumferential traction tests on coated and uncoated samples. The young modulus was calculated based on traction test data to obtain the compliance indirectly. Bustos et al have studied the mechanical characterization of a woven Dacron vascular graft [83]. They have performed uniaxial tensile tests under different orientations to obtain the anisotropic behavior of the material. They have also fitted the test data to a hyper elastic anisotropic constitutive model to be used through numerical simulations and predict mechanical response under ring tensile test.

Buckling in arteries and veins as the upshot of vascular instability plays a substantial role in the formation of several cardiovascular pathologies. Han et al. proposed a biomechanical model for the arterial buckling and developed a mathematical framework to analyze the effect of the internal pressure and torsion on the mechanics of arteries and veins using linear and nonlinear models for the first time [19-28]. They concluded that vascular buckling may occur due to the reduced axial strain, increased blood pressure and flexile wall material considering the alteration in the critical buckling pressure. Han and his coworkers also experimentally investigated the buckling behavior of arteries under torsion to determine the critical buckling torque, the critical buckling twist angle and the buckling shape [24]. They found that there is a strong correlation between the blood pressure and critical buckling twist angle although this relations has not mathematically been defined yet. After all, an *in-vitro* analysis of surgical configurations that has potential for buckling has not been studied in literature to our knowledge.

Therefore, this chapter is organized as follows; in the Methodology section, conduit materials and their preparation, uniaxial and biaxial test setups, linear and nonlinear least square fitting of material parameters for linear and nonlinear models are presented besides the calculation of critical buckling angle of the cylindrical conduits. In the Results section, least square fit for linear elastic model is performed using the uniaxial and biaxial tensile testing data, followed by calculation of critical buckling angle of idealized vessel geometries and the nonlinear materials of human and porcine pericardia appearing in Fung-type pseudo strain energy density function are determined. In the Discussions and Conclusions section, the capability and limitations of the proposed methods for examining conduit durability are analyzed in detail besides its possible future application on the non-invasive material characterization of human cardiovascular system.

3.2. Methods

3.2.1. Origin of Specimens and Their Preparation

PTFE and Dacron materials are synthetic materials and they are often used for blood vessel patches and cardiovascular surgeries because of their biocompatible properties. Small parts of specimens were taken out from the actual 20 mm diameter PTFE and Dacron conduits to be used in the pediatric cardiovascular surgeries. Human pericardium was only used for biaxial tensile test, where porcine pericardium was used both for uniaxial and biaxial tensile tests. The porcine pericardium was kept in glutaraldehyde solution was from (Edward Lifescineces). Human pericardium (age: 55, gender: male) was brought from Koc University Hospital, Istanbul, Turkey and tested with in the same day, through approved IRB.

Sample size 1 x 5 cm was cut out from the original Dacron and PTFE baffles and prepared for the uniaxial tests. Both circumferential and axial specimens were prepared for each material. Fats and tissues were removed from human pericardium before biaxial testing. 2 x 2 cm sized specimens were dotted with the tissue marker and connected to the test system using connecting hooks on the edges of the sample. These marks allow the camera system to detect and reconstruct strain data central to the sample (Figure 3.1).

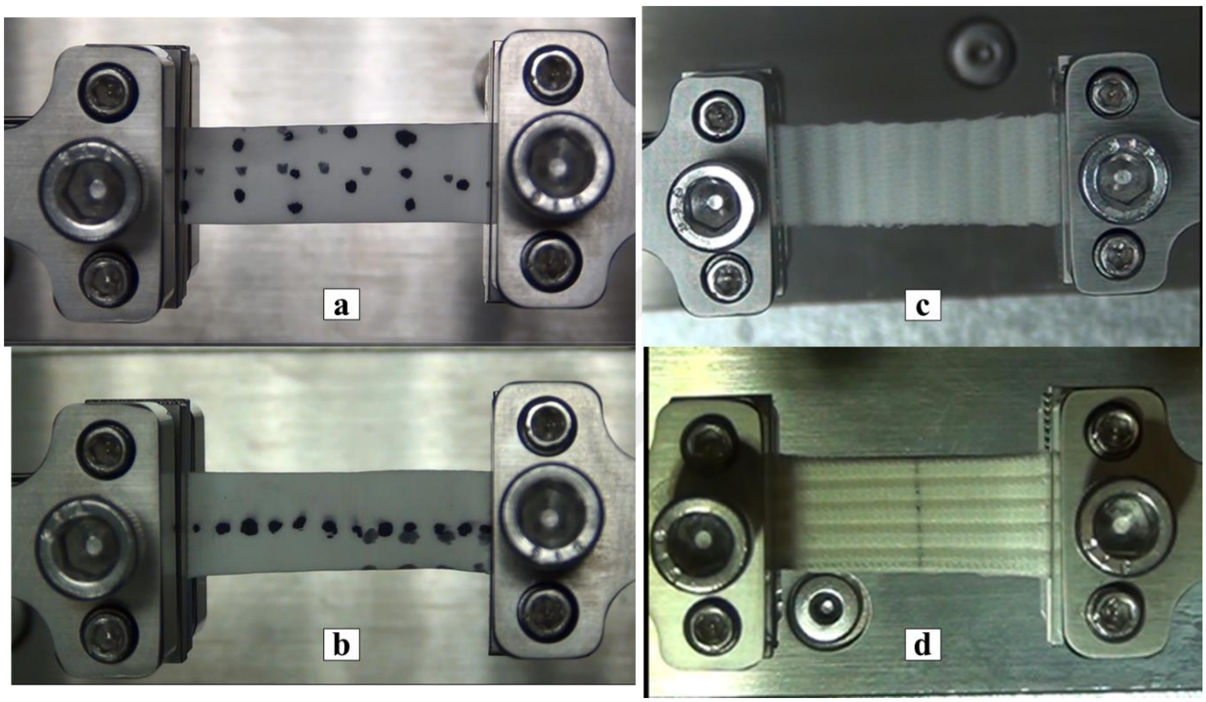

Figure 3.1: PTFE and ragged Dacron vessel segments are shown while placed on the uniaxial test setup clamps: in axial (a and c) and circumferential (b and d) directions, respectively.

3.2.2. Test Setups

A. Uniaxial Tensile Test Setup

Pincers were used for holding the specimen driven by high accuracy linear electromagnetic motors M1 (motor1) of the system. Specimens were fixed to the system by using larger size pincers and pulled in one axial direction at 0.001 mm/sec rate for 0.5 mm displacement at each ramp. We waited for 180 seconds at the end of the ramp. Ramp test was applied continuously 3 times and a total of 1.5 mm displacement was obtained while pulling the sample. Same protocol was used for both circumferential and longitudinal specimens. Specimen movement was recorded continuously and size was measured in each step.

B. Biaxial Tensile Test Setup

Porcine pericardium and human pericardium were connected to test system by using hooks on four edges (see Figure 3.2). Axial and circumferential alignments of the sample were considered as E11 (x axis) and E22 (y axis) respectively. Motors were moved backward carefully to remove the loosen part of the strings and pulled more until load cell value shows 0.7 N in both axis then load cells were zeroed in the software. 0.1 Hz. cycling test was applied to the specimens. Each cycle includes total 50 data points (25 for loading and 25 for unloading the sample) and total 100 cycle tests were applied to the specimens. Specimen net displacement was 4mm. for each direction and 40% stretching was applied. First 50 cycle data of the test was excluded for preconditioning and not used for analyze.

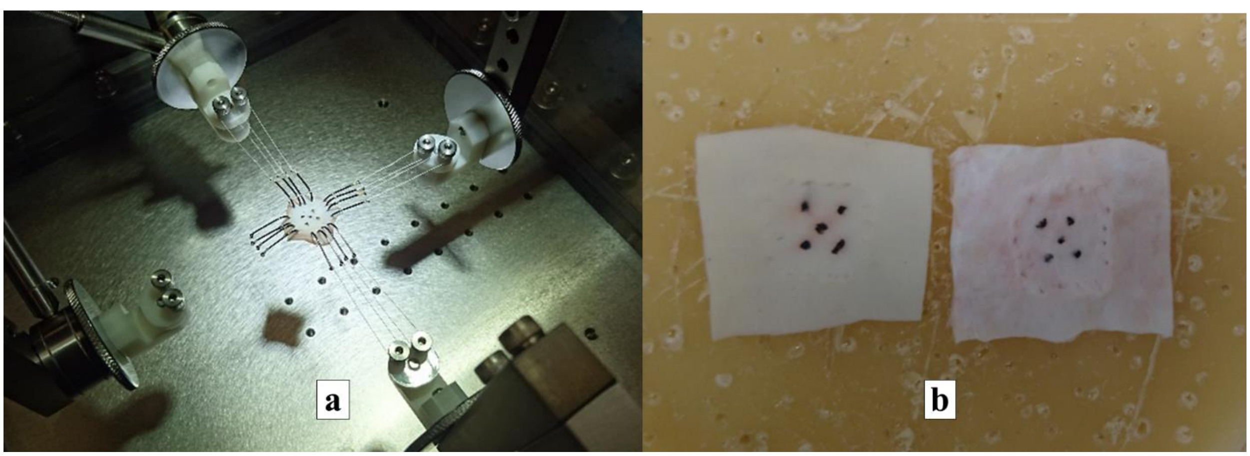

Figure 3.2: Biaxial tensile test setup with the human pericardium specimen placed for the experimental protocol (a) porcine and human pericardium specimens after being used in biaxial tensile test (b).

3.2.3. Linear Material Properties and Critical Buckling Twist Angle

A. Uniaxial and Biaxial Tensile Tests: Poisson's Ratio and Young's Modulus

The conduit material specimens (PTFE, Dacron and Pericard) are subjected to uniaxial tensile testing (BOSE planar biaxial test system, manufacturer: BOSE, Framingham, Massachusetts) to determine their Young's modulus. To this end, Young's modulus is computed by performing linear regression on stress-strain data set obtained from force-displacement measurements performed for each material.

All conduit material specimens were assumed to be homogeneous, isotropic and linear elastic. First, uniaxial tensile testing was performed on specimens of each material separately. Then linear regression was performed to compute Poisson's ratio values for each of them by using the following approximation.

$$\nu \approx \frac{\Delta L_y}{\Delta L_x} \tag{3.1}$$

Second, the average Young's Modulus values for the rectangular PTFE, Porcine Pericardium and Dacron specimens were computed separately by using the experimental data that were obtained by performing planar biaxial tensile testing. For this purpose, following two-dimensional stress formulas for the planar biaxial tensile testing were used.

$$\sigma_x = \frac{E(\varepsilon_x + \nu\varepsilon_y)}{1-\nu^2}, \sigma_y = \frac{E(\varepsilon_y + \nu\varepsilon_x)}{1-\nu^2} \tag{3.2}$$

where σ_x, σ_y and ε_x, ε_y are engineering stress and strain components in Cartesian coordinates, respectively. These stress and strain components are the arithmetic mean of values which are computed from force-displacement data by using the following relations.

$$\sigma_x = \frac{F_x}{tl_y}, \sigma_y = \frac{F_y}{tl_x} \tag{3.3}$$

Linear regression is performed on new parameters, which are defined below as sums of average stress and strain components separately, in order to compute the Young's modulus.

$$\sigma = \sigma_x^{'} + \sigma_y^{'} = \frac{E\left(w_1\varepsilon_x + w_2\varepsilon_y\right)}{1-\nu} = \frac{E\varepsilon}{1-\nu} \tag{3.4}$$

where w_1 and w_2 are weighting factors.

C. Critical Buckling Torque and Twist Angle

The critical buckling torque formula proposed for a linear elastic thin-walled cylinder subjected to a torque is given by [25]

$$T_{cr} = \frac{\pi\sqrt{2}E}{3\left(1-\nu^2\right)^{3/4}}\sqrt{Rt^5} \tag{3.5}$$

where E and ν are Young's modulus and Poisson's ratio values obtained from mechanical tests, and t and R are the thickness and radius (in a given pressure) of the cylindrical surgical conduit, respectively.

Neglecting the effect of collapse of planar cross-sectional area in the buckling region, mathematical relation between the critical buckling twist angle and torque can be given by

$$\varphi_{cr} = \frac{T_{cr}L}{GJ} \tag{3.6}$$

where L and J are length and polar moment of inertia, and G is the shear modulus of the cylindrical shell.

For a Hookean material, the mathematical relation between the shear modulus and Young's modulus is given by

$$G = \frac{E}{2\left(1+\nu\right)} \tag{3.7}$$

Substituting the Eq. (7) into the Eq. (6) the critical buckling twist angle formula is obtained as

$$\varphi_{cr} = \frac{2(1+\nu)T_{cr}L}{EJ} \tag{3.8}$$

3.2.4. Nonlinear Material Properties

A. Constitutive Equations and Nonlinear Least Squares Curve Fitting

Fung's 2D strain energy function is used to determine nonlinear properties of hyperelastic materials (mainly arteries) subjected to the biaxial tensile tests, which is given by [84]

$$W = \frac{1}{2}c\left(e^{Q}-1\right) \tag{3.9}$$

where $Q = a_1E_{11}^2 + a_2E_{22}^2 + 2a_3E_{11}E_{22}$

Also Green strains and stretch ratios are related by

$$E_{ii} = \frac{1}{2}\left(\lambda_i^2-1\right), i=1,2 \tag{3.10}$$

After some manipulations Cauchy stress components are obtained as

$$\sigma_{11} = \frac{1}{2}c\lambda_1^2\left[a_1\left(\lambda_1^2-1\right)+a_3\left(\lambda_1^2-1\right)\right]\cdot\exp\left[\frac{1}{4}\left(a_1\left(\lambda_1^2-1\right)^2+a_2\left(\lambda_2^2-1\right)^2+2a_3\left(\lambda_1^2-1\right)\left(\lambda_2^2-1\right)\right)\right]$$

$$\sigma_{22} = \frac{1}{2}c\lambda_2^2\left[a_2\left(\lambda_2^2-1\right)+a_3\left(\lambda_1^2-1\right)\right]\cdot\exp\left[\frac{1}{4}\left(a_1\left(\lambda_1^2-1\right)^2+a_2\left(\lambda_2^2-1\right)^2+2a_3\left(\lambda_1^2-1\right)\left(\lambda_2^2-1\right)\right)\right] \tag{3.11}$$

where c [Pa], a_1 [-], a_2 [-] and a_3 [-] are material parameters.

Cauchy stress components in 2D σ_{11} and σ_{22} expressed in terms of two variables-stretch ratios λ_1 and λ_2. In order to perform a nonlinear least squares curve fitting, $\{\lambda_1, \lambda_2\}$ are reduced to single variable $\lambda = \lambda_1$ and $\lambda_2 = k\lambda_1$, where k is determined by applying linear regression to the data set (λ_1, λ_2).

On the other hand, experimental stress values can be computed from force-displacement data using the following relations.

$$\sigma_{11}^{\exp} = \lambda_1 \frac{F_{11}}{b_2 t}, \quad \sigma_{22}^{\exp} = \lambda_2 \frac{F_{22}}{b_1 t} \tag{3.12}$$

where t is the thickness, b_1 and b_2 are orthogonal dimensions.

Objective function is defined as the root-mean-square deviation of Cauchy stress components from corresponding experimental values in 2D.

$$\min \left\| \vec{\sigma} - \vec{\sigma}^{\exp} \right\|_2 = \sqrt{\left(\sigma_{11} - \sigma_{11}^{\exp}\right)^2 + \left(\sigma_{22} - \sigma_{22}^{\exp}\right)^2} \tag{3.13}$$

Optimized material parameters are determined by minimizing the objective function.

3.3. Results

3.3.1 Linear Elastic Model

A. Poisson's Ratio and Young's Modulus Values

Linear regression is implemented to uniaxial tensile testing data and biaxial tensile testing data similarly using the Eq.(3.1) and stress function given in Eq.(3.4) in order to compute Poisson's ratio and Young's modulus, respectively, for PTFE, Dacron and porcine pericardium. Weighting factors in the Eq. (3.4) are determined as $w_1 = 1.00$ and $w_2 = 1.16$ and kept the same for each material to minimize the residual error in the objective function. All specimens are stretched up to ~%10 of its original length in order to examine nearly linear response of hyperelastic materials.

Results of the linear regression using biaxial tensile test data to determine Young's modulus for each material are given in Figure 3.3. Best simultaneously fitted linear regression is obtained for Dacron material among conduits. Fitted stiffness line for Dacron material matches the nonlinear test data with a relatively low error in both x and y directions. The error is relatively high and not within the acceptable range for other materials, especially the porcine pericardium due to its orthotropic behavior. Separately fitted Young's modulus in "x" and "y" directions produce a lower error for porcine pericardium compared to the simultaneously fitted Young's modulus. Neither simultaneous nor separate fitting technique produces an acceptable error range for PTFE material. We have tried dividing the stress strain data into two pieces and fitted two different Young's modulus to each region using simultaneous fitting technique. This decreased the error as can be seen in Figure 3.3. Although deformations in PTFE specimens are in the same order (linear region) as in Dacron and porcine pericardium specimens, fitted stress-strain curve is highly nonlinear whereas stress values in "x" and "y" directions are almost in the same order indicating isotropy. The relative error between the fitted curves and experimental data is up to %1000. It shows that the linear representation for the PTFE material is not an appropriate approach; it needs more elaborate treatment to examine the phenomenon of nonlinearity. Thus whole extension region for PTFE divided to three region; first region is low strain region where the engineering strain in x-direction is $\varepsilon_x = [0.0003 - 0.045]$ and second region is high strain region where the engineering strain in y-direction is $\varepsilon_x = [0.055 - 0.095]$. There is no sufficient number of experimental data in order to perform linear regression to third region, which has significantly different slope than other two regions have. This region can be considered as a starting point of nonlinear behavior. Linear regression is implemented into low strain and high strain regions in "x" and "y" directions separately to obtain E_{x1}, E_{x2} and E_{y1}, E_{y2}. For Dacron, the relative error in the linear regression is in acceptable range up to %37.5. Stress component in "y" direction is exponential-like where the "x" component looks like logarithmic unforeseeable. Moreover, unlike PTFE and Dacron, porcine pericardium is highly anisotropic in addition to its nonlinearity as seen in Figure 5. Maximum value of σ_y (0.5 MPa) is almost ten times greater than the maximum value of σ_x (0.05 MPa) for porcine pericardium. Hence linear regressions are performed separately for stresses in "x" and "y" directions, respectively.

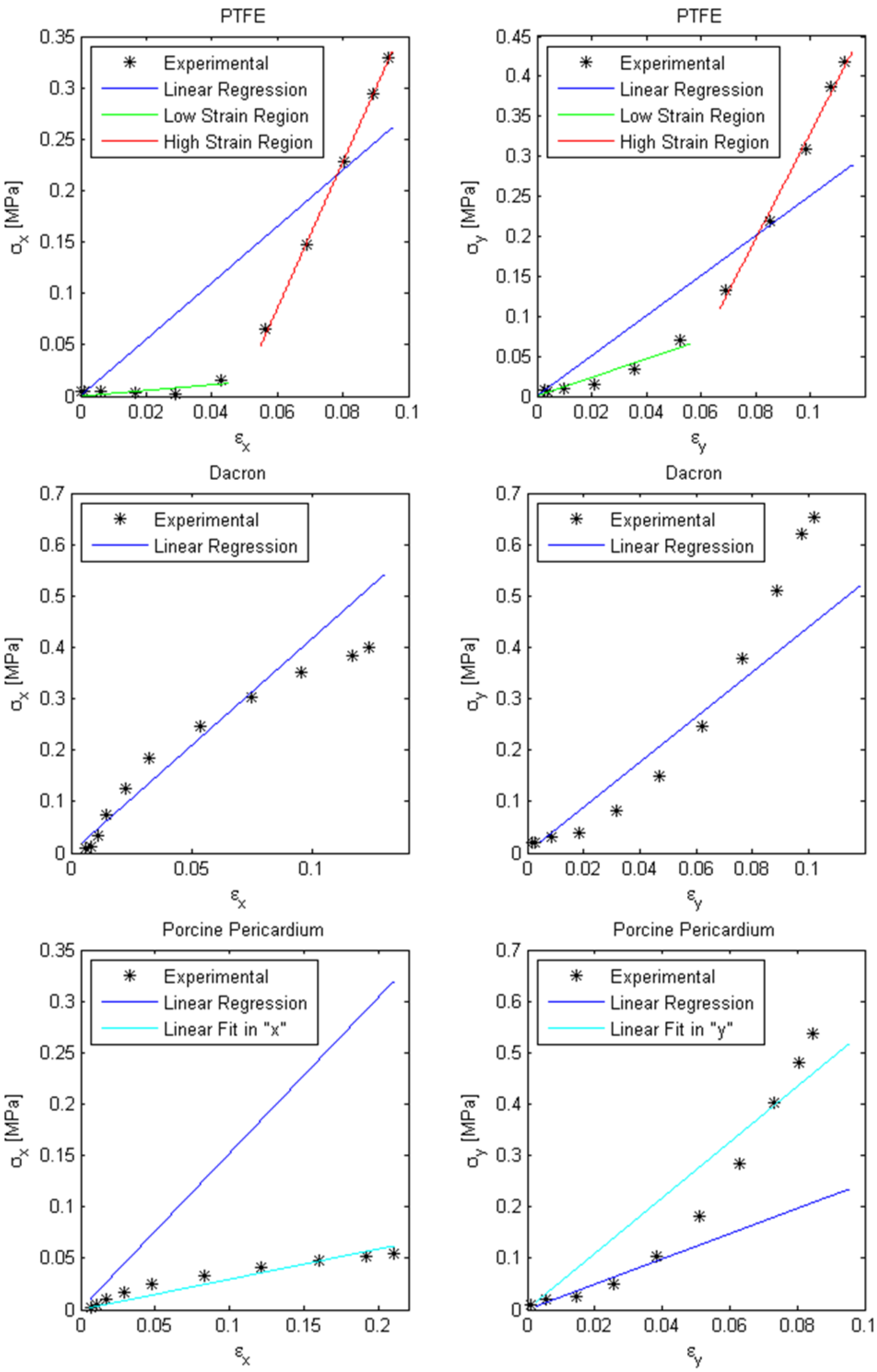

Figure 3.3: Experimental stress-strain data represented by stars which is computed from force-net displacement biaxial tensile testing data, which is obtained through for PTFE, Dacron and porcine pericardium. Blue lines are linear regression results obtained by least squares line fitting a line to this data of whole region in "x" and "y" directions for PTFE, Dacron and porcine pericardium, respectively. Green and red lines are fitted to the data of low strain and high strain regions for PTFE, respectively, in "x" and "y" directions separately. Cyan lines are separately fitted to whole stress-strain data in "x" and "y" directions, respectively.

Computed Poisson's ratio and Young's modulus values in whole range for PTFE, Dacron and porcine pericardium are given in Table 1. Note that computed Young's modulus values in low strain and high strain regions in "x" and "y" directions for PTFE are $E_{x1} = 0.182\,\text{MPa}$, $E_{x2} = 4.695\,\text{MPa}$ and $E_{y1} = 0.842\,\text{MPa}$, $E_{y2} = 4.778\,\text{MPa}$, respectively. In addition, Young's modulus values in "x" and "y" directions for porcine pericardium are computed as $E_x = 0.204\,\text{MPa}$ and $E_y = 2.315\,\text{MPa}$, respectively. Porcine pericardium is the least stiff material, especially in the circumferential direction while Dacron is found to be the stiffest material. All of the materials are in the compressible region.

Table 3.1. Poisson's ratio and Young's modulus values for PTFE, Dacron and porcine pericardium are computed.

	PTFE	Dacron	Porcine Pericardium
Poisson's Ratio [-]	0.31	0.39	0.42
Young's Modulus [MPa]	1.807	2.601	1.050

B. Critical Buckling Twist Angle

The critical buckling twist angle values at 3, 6, 9, 12, 15 mmHg are measured to represent the inferior vena cava pressure range for each material. The value at 0 mmHg is extrapolated from measured values. Thereafter extrapolated values were compared with the computed values appearing in Table 3.2.

Table 3.2. Computed critical buckling twist angle values were compared with the values of critical buckling twist angle extrapolated at 0 mmHg by using the experimentally measured values for PTFE, Dacron and porcine pericardium.

		PTFE	Dacron	Porcine Pericardium
Critical Buckling Angle (degrees)	Computed at 0mmHg	7.7	8.6	9.0
	Extrapolated at 0mmHg	10.3	12.6	3.2
	Measured under 3 mmHg	17.2	18.9	7.1
	Measured under 6 mmHg	22	22.1	10.7
	Measured under 9 mmHg	29.1	26	13.8
	Measured under 12 mmHg	30.9	31.3	33.9
	Measured under 15 mmHg	43	39.1	62

Linear correlation is observed between the critical buckling twist angle and blood pressure after examining the Table 3.2. in detail. Linear extrapolation was applied to the arithmetic mean of the experimentally measured (at 3, 6, 9, 12 and 15 mmHg) pressure – critical buckling twist angle data points for PTFE, Dacron and porcine pericardium to estimate the critical buckling twist angle at 0 mmHg. Hence linear regression is implemented to the critical buckling twist angle-blood pressure $\varphi_{cr} - p$ data sets for PTFE, Dacron and porcine pericardium to demonstrate this correlation $\varphi_{cr} = \kappa_1 p + c$ as given in Figure 4. Amazingly, direct proportionality is found between coefficients $\kappa_1 = (\varphi_{cr} - c)/p$ and $\kappa_2 = (1+\nu)/E$ from the Eq.(3.5) whereas polar inertial moment J and length of the cylindrical tube of each material are the same, and blood pressure is proportional to critical torque ($p \propto T_{cr}(p)$) since the blood pressure p may induce additional torque T_{add}, which is embedded in net critical torque at some pressure p, $T_{cr}(p) = T_{cr}(0) + T_{add}$ due to the wrinkles produced in the arterial wall while the torsion is applied to cylindrical tubes. Computed κ_1 and κ_2 values for each material are given in Table 3.3.

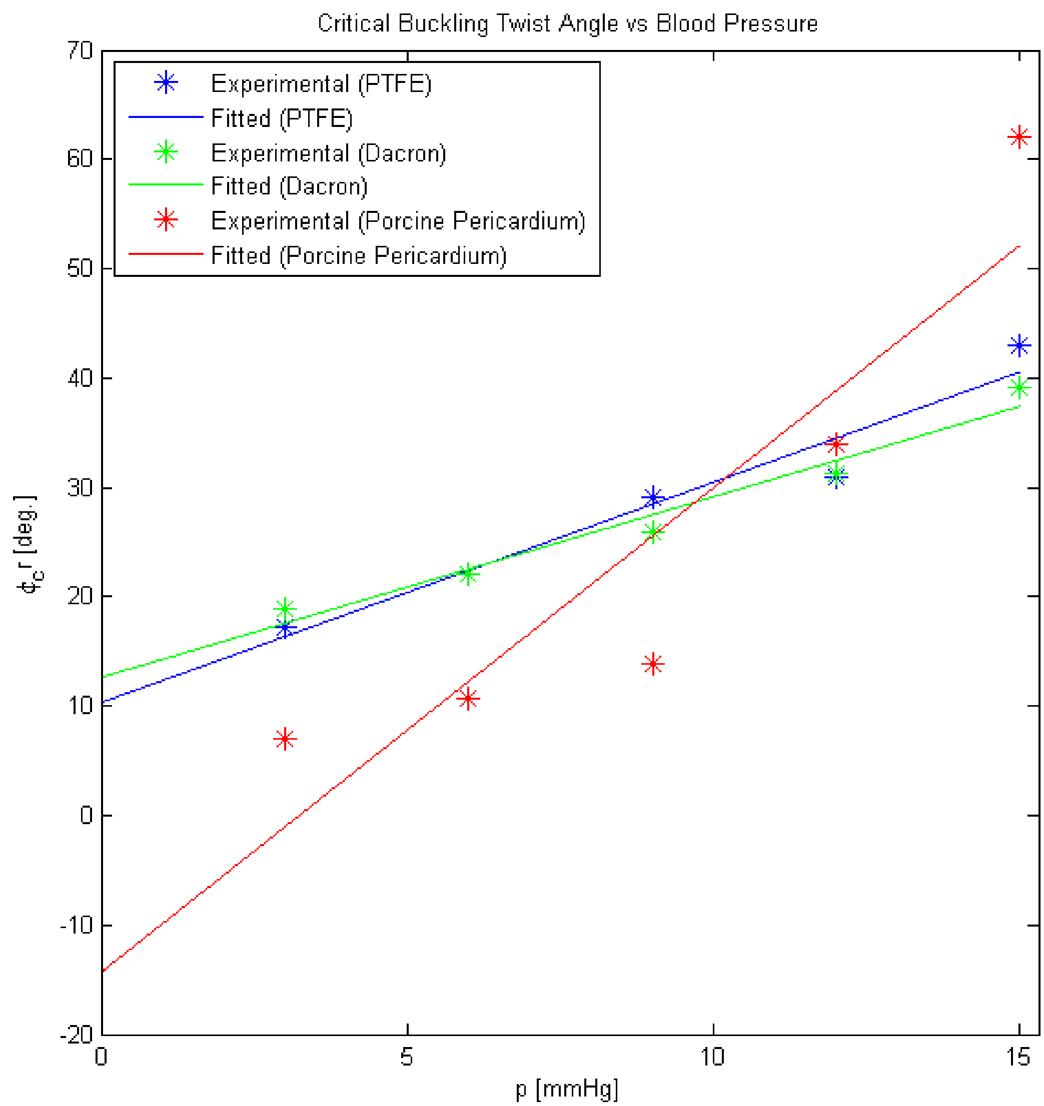

Figure 3.4: Linear regression is implemented separately to the critical buckling twist angle-blood pressure data sets for PTFE, Dacron and porcine pericardium experimentally measured at 3 mmHg, 6 mmHg, 9 mmHg, 12 mmHg and 15 mmHg, respectively.

Table 3.3. Coefficients κ_1 and κ_2 are computed for PTFE, Dacron and porcine pericardium using Poisson's ratio and Young's modulus values of each from Table 3.1.

	κ_1	κ_2
PTFE	2.02	7.25e-07
Dacron	1.65	5.34e-07
Porcine Pericardium	4.43	1.35e-06

Both κ_1 and κ_2 are the greatest for porcine pericardium, then less for PTFE and the least for Dacron.

3.2 Fung's 2D Pseudo Strain Energy Function

The force-displacement data obtained produced by biaxial tensile testing are converted into stress-strain data and fitted to the Fung's 2D SEF for human and porcine pericardium. The resulting nonlinear material parameters are given in Table 3.4 together with literature values for material parameters of human intracranial blood vessel [84]. Figure 3.5 presents the measured data and the curves fitted to the data in axial and circumferential directions. There can be seen two regions in the figures. First region covers approximately the 20% strain of segment and represents the relatively linear behavior of the material. Second region is the higher strain (>20%) zone and starts showing a relatively nonlinear behavior. The difference (error) between measured data and fitted curve in the first region is higher (up to 1000%) compared to that of the second region due to the nonlinear nature of the strain energy density function. Especially the part of the data, which is higher than 30% strain, fits to the nonlinear curve with a very low error.

Table 3.4. Computed material parameters of porcine pericardium and human pericardium

appearing in Fung's 2D pseudo strain energy function and literature values of human intracranial blood vessel are given.

Material Type	c [MPa]	a_1 [-]	a_2 [-]	a_3 [-]
Porcine Pericardium	2.39	0.0532	0.0000	0.7197
Human Pericardium	0.0448	6.7999	5.5671	0.0000
Human Intracranial Blood Vessel [84]	0.313	2.898	1.186	0.130

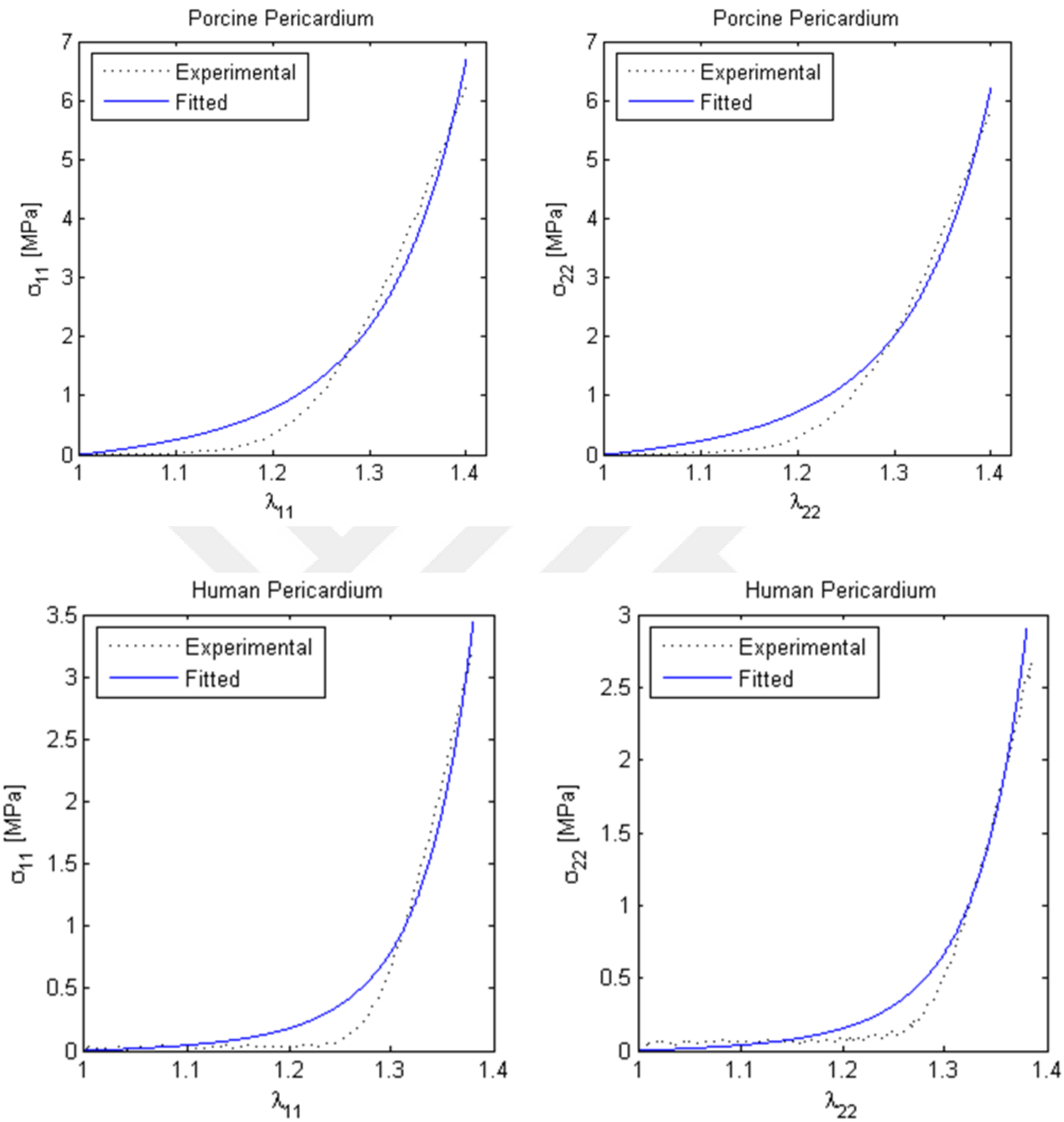

Figure 3.5: Nonlinear least-squares curve fitting is implemented to experimental stress-stretch ratio data in "x" and "y" directions for porcine and human pericardia, respectively. Force-net displacement data sets were obtained by using biaxial tensile tests.

3.4. Discussion

Biaxial tensile testing is one of common ways to determine the mechanical properties of materials. It is suitable to determine both linear and nonlinear elastic responses. Obviously, hyperplastic materials demonstrate linear response at small stresses and become nonlinear as the applied force increases. For instance, soft tissues such as arteries and veins shows linear elastic response at small blood pressures due to elastin fibers and other extracellular components since collagen fiber becomes active at high pressures. Therefore, average stiffness of hyperplastic materials can be computed by using linear model at small stresses. Besides, homogeneity and isotropy are other approximations to the realistic material in order simplify the case and provide rough estimations about the stiffness of the material where, in fact, the material itself may be nonhomogeneous and anisotropic up to some acceptable degree. In this study we showed that PTFE is highly nonlinear even in small deformations. For Dacron, logarithmic shape of the stress component in "x" direction can be associated with ragged shape of the Dacron specimen. Usually, logarithmic stress response is seen in metals as the elastic region gives place to the plastic region via necking. However in this case, the logarithmic shape occurs due the opening of the ragged structure of the Dacron material. Furthermore, while the assumption of anisotropy is viable for PTFE and Dacron, porcine pericardium is highly anisotropic as it can be seen from Figure 3.3.

Although there is no direct analytical relation binding the internal pressure to the critical buckling twist angle, by looking closely at Eq. (7) it can be roughly commented that increasing blood pressure creates an additional positive moment which in return linearly increases the critical buckling twist angle. The additional positive moment is probably produced due to unsymmetrical material surface. Tangential component of the force field determined by integrating the internal pressure over inner surface area creates the additional positive moment increasing the resistivity of the material to the twist buckling. Furthermore, relative error between theoretically computed and extrapolated values of critical buckling twist angle at 0 mmHg is in the range of 25% – 63%. Higher relative error in critical buckling twist angle values for the porcine pericardium is due to the experimental limitations (very unstable and sensitive response of the tissue to very low twist angle deformations). On the other hand, relative error in critical buckling twist angle for PTFE and Dacron is in the acceptable range being 25% and 40%, respectively.

Despite the fact that the assumptions of homogeneous, isotropic and linear elastic materials do not seriously affect the applicability of simple technique to compute the critical buckling twist angle, using orthotropic hyperplastic models would give more precise results. In addition, it may be though that the assumption of planar cross-sectional area is a weak claim since it may not represent the real case. In fact, this assumption helps us to predict the critical twist buckling angle earlier than the buckling occurs which in return gives an advantage to surgeons in selecting the buckling resistive materials before surgical operations.

In addition, comparison of computed material parameters of porcine pericardium with computed material parameters of human pericardium and literature values for those of human intracranial blood vessel appearing in Fung's 2D pseudo strain energy function provides an information about the incompatibility of the porcine pericardium as the vascular conduit since there is a sharp transition in the material stiffness at the boundaries of two different materials creating a significant discontinuity in stress distribution.

Unfortunately, to date there are very few experimental data of human heart tissues available to estimate material parameters and to develop adequate material models. Sommer et al [77] aimed in their study to determine biaxial extension and triaxial shear properties and the underlying microstructure of the passive human ventricular myocardium. Using new state-of-the-art equipment, they performed planar biaxial extension tests to determine the biaxial extension properties of the passive ventricular human myocardium. In the present thesis we also performed biaxial extension properties of human pericardium and contribute to further understand the complex nonlinear behavior of the human tissue. As a future work, presented mathematical technique will allow noninvasive *in vivo* determination of nonlinear material parameters together with residual strain parameters of human cardiovascular system introduced in previous study [16]. It can be used to fully analyze three-dimensional characterization of hyperelastic materials including residual stresses.

Chapter 4 Optimal Material Parameters to Attain a Uniform Stress Distribution in Growing and Remodeling Arteries

Evolution of biological systems can be considered analogous to an optimization problem minimizing the governing biomechanical properties at every time step. The physiological course of this process involves a wide range of temporal scales. Arteries that are developing can alter their 3D shapes and microstructure in such a way that the stress distribution through the arterial wall is nearly uniform. This state corresponds to the most cost-effective load carrying configuration. For this purpose, sizes and material properties of arteries are optimized (grown or remodeled) to make the stress distribution as much as uniform as it can. Two-layer orthotropic fiber-reinforced strain energy function introduced by Holzapfel and Gasser is used as a constitutive relation [15].

4.1. Holzapfel-Gasser-Ogden Microstructure Model

Arteries consist of three main layers namely (tunica) intima, media and adventitia, Figure 4.1. Intima is a very thin layer comprised of one layer of endothelial cells and supported by internal elastic lamina. In HGO model (Holpzapfel-Gasser-Ogden model), the intima layer is not taken into account since it does not bear significant mechanical loading, so that it has negligible contribution to the total mechanical response. Media layer in large arteries are mostly comprised of circular and longitudinal smooth muscle fibers and elastic fibers (bundles of proteins known as elastin). The adventitia is the outer layer and it is thinner than the media. It is composed of collagen fibers and supported by external elastic lamina.

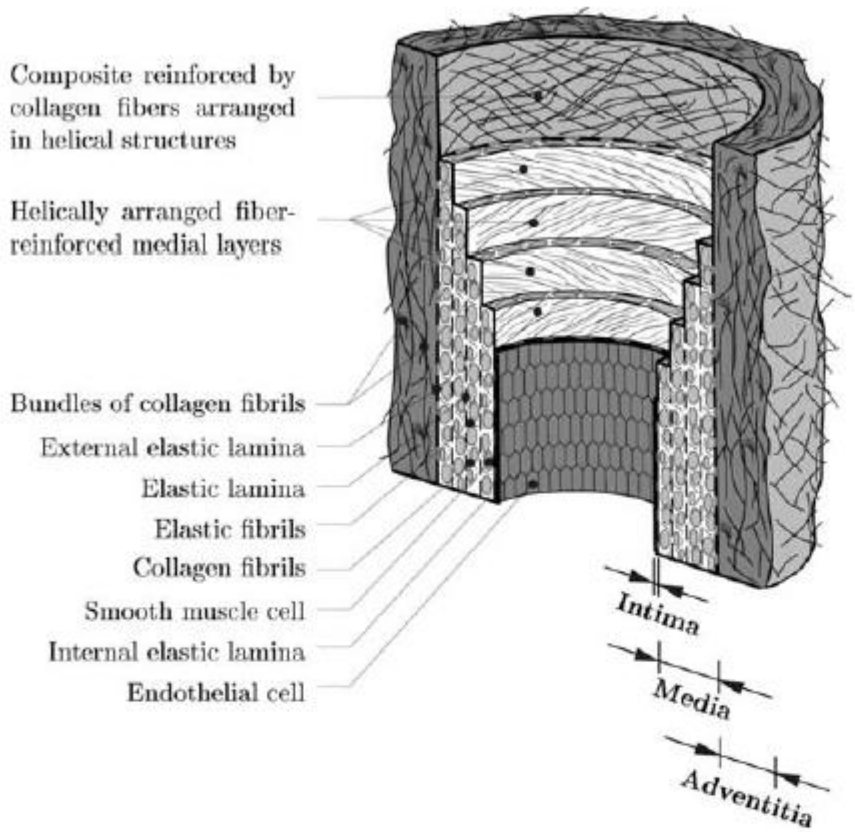

Figure 4.1: Diagrammatic model of the major components of a healthy *elastic* artery composed of three layers: intima (**I**), media (**M**), adventitia (**A**). **I** is the innermost layer consisting of a single layer of endothelial cells that rests on a thin basal membrane and a subendothelial layer whose thickness varies with topography, age and disease. **M** is composed of smooth muscle cells, a network of elastic and collagen fibrils and elastic laminae which separate **M** into a number of fiber-reinforced layers. The primary constituents of **A** are thick bundles of collagen fibrils arranged in helical structures; **A** is the outermost layer surrounded by loose connective tissue [15].

4.1.1. Kinematics

Arteries are considered as an incompressible thick-walled cylindrical tube subject to various modes of mechanical loading. As discussed in Chapter 2, 2.2.1 Representation of the Vascular Loading States, there are three main states of arteries under the effect of internal pressure and axial tensile force such as stress-free state, unloaded state and loaded state. Torsional effect can also be included but in this study the torsional kinematic contribution is not included in the formulation.

In cylindrical coordinates the geometrical domain of artery is defined by

$$R_i \le R \le R_o,\ 0 \le \Theta \le 2\Theta_0,\ 0 \le Z \le L \tag{4.1}$$

where R_i, R_o, Θ_0 and L are the inner and outer radii, the effective angle [11] and length of the tube is recorded at the original "stress-free" configuration. The effective angle Θ_0 is defined earlier by Eq.(2.1)

In deformed configuration, the geometrical domain becomes

$$r_i \leq r \leq r_o,\ 0 \leq \theta \leq 2\pi,\ 0 \leq z \leq l \tag{4.2}$$

where r_i, r_o and l are the inner and outer radii, and length of the tube in the deformed configuration.

Likewise, the deformed axial coordinate is $z = \lambda_z Z$ and deformed radial coordinate r is expressed in the Eq.(2.1). In the presence of twist, the circumferential coordinate θ is given by

$$\theta = \frac{\pi\Theta}{\Theta_0} + Z\frac{\Phi}{L} \tag{4.3}$$

where Φ is the angle of twist occurring due to the torsion.

In addition to the principal stretch ratios λ_r , λ_θ and λ_z (Eq.(2.1)) when there is no twist, γ is the local amount of shear in a *(θ, z)* plane.

$$\gamma = r\frac{\partial\theta}{\partial z} = r\frac{\Phi}{l} \tag{4.4}$$

In this study, there is no torsion, so that there is no twist and no shear $\gamma=0$.

Note that the incompressibility condition implies that

$$J = 1 \text{ and } \lambda_z\lambda_\theta\lambda_z = 1 \tag{4.5}$$

4.1.2. Static Equilibrium

In general, the equation of equilibrium is given by

$$div\sigma = 0 \tag{4.6}$$

Due to the axial symmetry in cylindrical coordinates *(r, θ, z)* only the radial component of the divergence survives.

$$\frac{d\sigma_{rr}}{dr} + \frac{(\sigma_{rr} - \sigma_{\theta\theta})}{r} = 0 \tag{4.7}$$

Applying the boundary conditions $\sigma_{rr}|_{r=r_o} = 0$, where the osmotic pressure on the outer surface is assumed to be zero, and $\sigma_{rr}|_{r=r_i} = -p_i$, where p_i is the internal pressure. Thus, the pressure equation is obtained by

$$p_i = \int_{r_i}^{r_o} \frac{(\sigma_{\theta\theta} - \sigma_{rr})}{r'} dr', \; r_i \le r \le r_o \tag{4.8}$$

The axial force *s* and the torque M_t are given by

$$N = 2\pi \int_{r_i}^{r_o} \sigma_{zz} r dr, \; M_t = 2\pi \int_{r_i}^{r_o} \overline{\sigma}_{\theta z} r^2 dr \tag{4.9}$$

Since $\sigma_{\theta\theta} = p + \overline{\sigma}_{\theta\theta}$ and $\sigma_{rr} = p + \overline{\sigma}_{rr}$ (see 4.2.3 Constitutive Relations for details) the Eq.(4.8) can be rewritten as follows.

$$p_i = \int_{r_i}^{r_o} \frac{(\overline{\sigma}_{\theta\theta} - \overline{\sigma}_{rr})}{r'} dr' = 0 \tag{4.10}$$

This pressure integral is again solved numerically using the Gaussian quadrature introduced in the Eq.(2.13).

4.1.3. Constitutive Relations

In this model each layer media and adventitia contains two families of collagen fibers which are symmetrical helixes. This kind of simplified engineering approach allow us to model the passive mechanical response of the arterial tissue instead of formulating more complicated active response resulting from the contraction of the smooth muscle cells present in the media.

Collagen fibers are stiffer thousand times more than elastic fibers and other extra cellular matrix component. Thus nonlinear behavior becomes evident at higher pressure values as collagen fibers start to be stretched. Note that collagen fibers do bear only tensile loading as other linear elastic components do.

In general, strain energy function is defined as Helmholtz free energy, which is a sum of volumetric and isochoric parts.

$$\Psi(E, A_1, A_2, ..., A_n) = U(J) + \overline{\Psi}(\overline{E}, A_1, A_2, ..., A_n) \tag{4.11}$$

where U is the volumetric part depending on the local volume ratio and $\overline{\Psi}$ is the isochoric part of the free energy Ψ.

For an adiabatic process, Piola-Kirchoff stress tensor is obtained by taking the derivative of the Helmholtz free energy with respect to the Green strain tensor according to the Clausius-Planck inequality.

$$S = \frac{\partial \Psi(E, A_1, A_2, ..., A_n)}{\partial E} \tag{4.12}$$

where

$$S = S_{vol} + \overline{S},\ S_{vol} = \frac{\partial U(J)}{\partial E} \text{ and } \overline{S} = \frac{\partial \overline{\Psi}(\overline{E}, A_1, A_2, ..., A_n)}{\partial E} \tag{4.13}$$

Note that

$$\frac{\partial J}{\partial E} = JC^{-1} \text{ and } \frac{\partial \overline{E}}{\partial E} = J^{-2/3}\left(\mathrm{I} - \frac{1}{3}\overline{C} \otimes \overline{C}\right) \tag{4.14}$$

where I is the fourth-order identity tensor in the form of $\mathrm{I}_{ijkl} = (\delta_{ik}\delta_{jl} + \delta_{il}\delta_{jk})/2$.

Then S_{vol} and $\bar{S}$ can be rewritten as

$$S_{vol} = HJC^{-1} \text{ and } \overline{S} = J^{-2/3} Dev\left(\frac{\partial \overline{\Psi}}{\partial E} \right) \quad (4.15)$$

where H is a hydrostatic pressure $H = \dfrac{\partial U}{\partial J}$. In case of incompressible material the hydrostatic pressure H becomes an indeterminate Lagrange multiplier which will be determined later after introducing static boundary conditions.

In Lagrangian description the deviatoric operator is defined by

$$Dev(\bullet) = (\bullet) - \frac{1}{3}\left[(\bullet) : \overline{C}\right]\overline{C}^{-1} \quad (4.16)$$

The Cauchy stress tensor is obtained from Piola-Kirchoff stress tensor by performing coordinate transformation.

$$\sigma = J^{-1} FSF^{T} \quad (4.17)$$

Then the volumetric and isochoric part of Cauchy stress tensor separately becomes

$$\sigma_{vol} = HI \text{ and } \overline{\sigma} = J^{-1} dev\left(\overline{F} \frac{\partial \overline{\Psi}}{\partial \overline{E}} \overline{F}^{T} \right) \quad (4.18)$$

where the total Cauchy stress tensor is $\sigma = \sigma_{vol} + \overline{\sigma}$.

Here the deviatoric operator is in its Eulerian description given by

$$dev(\bullet) = (\bullet) - \frac{1}{3}\left[(\bullet) : I\right] I \quad (4.19)$$

In this model the strain energy function is the same for each layer where material parameters are different. The isochoric part of the Helmholtz free energy (strain energy function) $\overline{\Psi}$ can be written as a linear superposition of isotropic part $\overline{\Psi}_{iso}$ corresponding to the linear elastic response of (non-collagenous) matrix material at low pressures and anisotropic part $\overline{\Psi}_{aniso}$ corresponding to the nonlinear behavior of collagen fibers at high pressures since wavy collagen fibers is not active at low pressures and become significant at high pressures. Remember that collagen fibers are significantly more stiffer than elastic fiber, so that the effect elastic fibers is included in the isotropic part, but can be included similarly if needed.

Hence, the isochoric part of the Helmholtz free energy is written as

$$\overline{\Psi}\left(\overline{C}, a_{01}, a_{02}\right) = \overline{\Psi}_{iso}\left(\overline{C}\right) + \overline{\Psi}_{aniso}\left(\overline{C}, a_{10}, a_{20}\right) \tag{4.20}$$

Eq.(4.20) can be written in its reduced form since $\bar{I}_3$, $\bar{I}_9$ are constants.

$$\overline{\Psi}\left(\overline{C}, A_1, A_2\right) = \overline{\Psi}_{iso}\left(\bar{I}_1, \bar{I}_2\right) + \overline{\Psi}_{aniso}\left(\bar{I}_1, \bar{I}_2, \bar{I}_4, \ldots, \bar{I}_8\right) \tag{4.21}$$

where $\bar{I}_4$ and $\bar{I}_6$ are squares of the stretches in the direction a_{01} and a_{02}, respectively. These vectors represent directions of two families of collagen fibers.

Eq.(4.21) can be simply written as

$$\overline{\Psi}\left(\overline{C}, A_1, A_2\right) = \overline{\Psi}_{iso}\left(\bar{I}_1\right) + \overline{\Psi}_{aniso}\left(\bar{I}_4, .\bar{I}_6\right) \tag{4.22}$$

The neo-Hookean model is used to define the isotropic part of the function for each layer.

$$\overline{\Psi}_{iso}\left(\bar{I}_1\right) = \frac{c}{2}\left(\bar{I}_1 - 3\right) \tag{4.23}$$

where c is a positive number, material parameter in the dimension of stress [kPa]. At higher pressure exponential shape of the mechanical response becomes dominant over the linear one.

$$\overline{\Psi}_{aniso}\left(\bar{I}_4, \bar{I}_6\right) = \sum_{i=4,6}\left\{\exp\left[k_2\left(\bar{I}_i - 1\right)^2\right] - 1\right\} \tag{4.24}$$

where k_1 is also a positive stress-like material parameters as c and k_2 is also positive but dimensionless parameter.

Eulerian description provides physically measurable quantities like Cauchy stress tensor. The isochoric part $\bar{\sigma}$ of the Cauchy stress tensor is determined by

$$\bar{\sigma} = c\,dev\left(\bar{b}\right) + \sum 2\bar{\Psi}_i\, dev\left(a_i \otimes a_i\right) \tag{4.23}$$

where $\bar{\Psi}_4 = \partial\bar{\Psi}_{aniso} / \partial\bar{I}_4$, $\bar{\Psi}_6 = \partial\bar{\Psi}_{aniso} / \partial\bar{I}_6$ stand for scalar response functions and $a_i = \bar{F}a_{0i}, i = 1{,}2$ are a_{0i} in Eulerian description.

The HGO model has 6 material parameters such c_M, k_{1M}, k_{2M} for the media and c_A, k_{1A}, k_{2A} for the adventitia. For two-layer thick-walled cylindrical tube the isochoric part of the Helmholtz free energy for each layer is given by

$$\bar{\Psi}_M = \frac{c_M}{2}\left(\bar{I}_1 - 3\right) + \frac{k_{1M}}{2k_{2M}} \sum_{i=4,6} \left\{ \exp\left[k_{2M}\left(\bar{I}_{iM} - 1\right)^2 - 1 \right] \right\},\ R_i \le R \le Ri + t_M$$

$$\bar{\Psi}_A = \frac{c_A}{2}\left(\bar{I}_1 - 3\right) + \frac{k_{1A}}{2k_{2A}} \sum_{i=4,6} \left\{ \exp\left[k_{2A}\left(\bar{I}_{iA} - 1\right)^2 - 1 \right] \right\},\ R_i + t_M \le R \le R_o \tag{4.24}$$

where t_M is the reference thickness of the media and $\bar{I}_{4j} = A_{1j} : \bar{C}$ and $\bar{I}_{6j} = A_{2j} : \bar{C}$ are the invariants corresponding to the media M and the adventitia A for $j = M, A$ respectively. A_{1j} and A_{2j} are the tensors representing the fiber directions.

$$A_{1j} = a_{01j} \otimes a_{01j},\ A_{2j} = a_{02j} \otimes a_{02j} \ \text{ for } \ j = M, A \tag{4.25}$$

where a_{01j} and a_{02j} are vectors expressed in cylindrical coordinates.

$$a_{01j} = \begin{bmatrix} 0 \\ \cos\beta_j \\ \sin\beta_j \end{bmatrix},\ a_{02j} = \begin{bmatrix} 0 \\ \cos\beta_j \\ -\sin\beta_j \end{bmatrix} \ \text{ for } \ j = M, A \tag{4.26}$$

where βj , $j=M, A$ are the half of the angles between two helical collagen fibers in media and adventitia, respectively.

After this point intermediate steps in the derivation of Eq.(4.23) will follow.

The deformation gradient tensor for the incompressible material $J=1$

$$F = F^T = \begin{pmatrix} (\lambda_\theta \lambda_z)^{-1} & 0 & 0 \\ 0 & \lambda_\theta & 0 \\ 0 & 0 & \lambda_z \end{pmatrix} \tag{4.27}$$

Then left Cauchy-Green tensor becomes

$$b = b^T = F \cdot F^T = \begin{pmatrix} (\lambda_\theta \lambda_z)^{-2} & 0 & 0 \\ 0 & \lambda_\theta^2 & 0 \\ 0 & 0 & \lambda_z^2 \end{pmatrix} \tag{4.28}$$

The deviatoric of $\bar{b}$ is given by

$$dev(\bar{b}) = \begin{pmatrix} (\lambda_\theta \lambda_z)^{-2} - \bar{b} : I/3 & 0 & 0 \\ 0 & \lambda_\theta^2 - \bar{b} : I/3 & 0 \\ 0 & 0 & \lambda_z^2 - \bar{b} : I/3 \end{pmatrix} \tag{4.29}$$

where

$$\bar{b} : I = (\lambda_\theta \lambda_z)^{-2} + \lambda_\theta^2 + \lambda_z^2 = tr(\bar{b}) \tag{4.30}$$

There is an Einstein summation over the repeated index "*i*".

$$dev(\vec{a}_i \otimes \vec{a}_i) = dev\left[\sum_{i=1}^{2} \vec{a}_i \otimes \vec{a}_i\right] = A - \frac{1}{3}[A : I]I \tag{4.31}$$

where

$$A = \sum_{i=1}^{2} \vec{a}_i \otimes \vec{a}_i = \begin{pmatrix} 0 & 0 & 0 \\ 0 & 2(\lambda_\theta \cos\beta)^2 & 0 \\ 0 & 0 & 2(\lambda_z \sin\beta)^2 \end{pmatrix} \tag{4.32}$$

and

$$A : I = tr(A) = 2(\lambda_\theta \cos\beta)^2 + 2(\lambda_z \sin\beta)^2 \tag{4.33}$$

Invariants $\bar{I}_4$ and $\bar{I}_6$ are obtained by

$$\bar{I}_4 = \bar{I}_6 = \lambda_\theta^2 \cos^2 \beta + \lambda_z^2 \sin^2 \beta \qquad (4.34)$$

Consequently, $\bar{\Psi}_4$ and $\bar{\Psi}_6$ become

$$\bar{\Psi}_4 = \frac{\partial \bar{\Psi}_{aniso}}{\partial \bar{I}_4} = k_1 \left\{ \left(\bar{I}_4 - 1 \right) \exp \left[k_2 \left(\bar{I}_4 - 1 \right)^2 \right] \right\} \text{ and } \bar{\Psi}_6 = \frac{\partial \bar{\Psi}_{aniso}}{\partial \bar{I}_6} = k_1 \left\{ \left(\bar{I}_6 - 1 \right) \exp \left[k_2 \left(\bar{I}_6 - 1 \right)^2 \right] \right\} \quad (4.35)$$

Up to this point the deviatoric stress tensor is obtained analytically.

Next, the hydrostatic is given by

$$H(r) = -\bar{\sigma}_{rr}(r) - L(r) + K \qquad (4.36)$$

where $L(r) = \int_r^{r_o} \frac{\left(\bar{\sigma}_{\theta\theta} - \bar{\sigma}_{rr} \right)}{r'} dr'$ and K is an integration constant is $K=0$ due to the boundary conditions.

4.1.4 Stress Distribution

Cauchy stress components are computed through the thickness of inflated tube-like carotid artery subjected to the internal pressure of 13.3 [kPa] with $\lambda_z = 1.7$ and $\gamma = 0$ without residual strains ($\Theta_0 = 180^0$) and with residual strains ($\Theta_0 = 100^0$) using Gaussian quadrature method with 6 nodes giving more precise results than those Holzapfel et al. obtained using 3 nodes. Note that Gaussian quadrature is used to compute the pressure integral Eq.(4.10) numerically, which is not analytically integrable, then to compute stresses.

For this purpose, inner radius values of rabbit carotid artery computed by using 3 nodes at 13.33 kPa and 15 kPa without and with residual strains are digitized from pressure-inner radius graph given in Figure 4.2. Inner radius values are presented in Table 4.1.

(a)

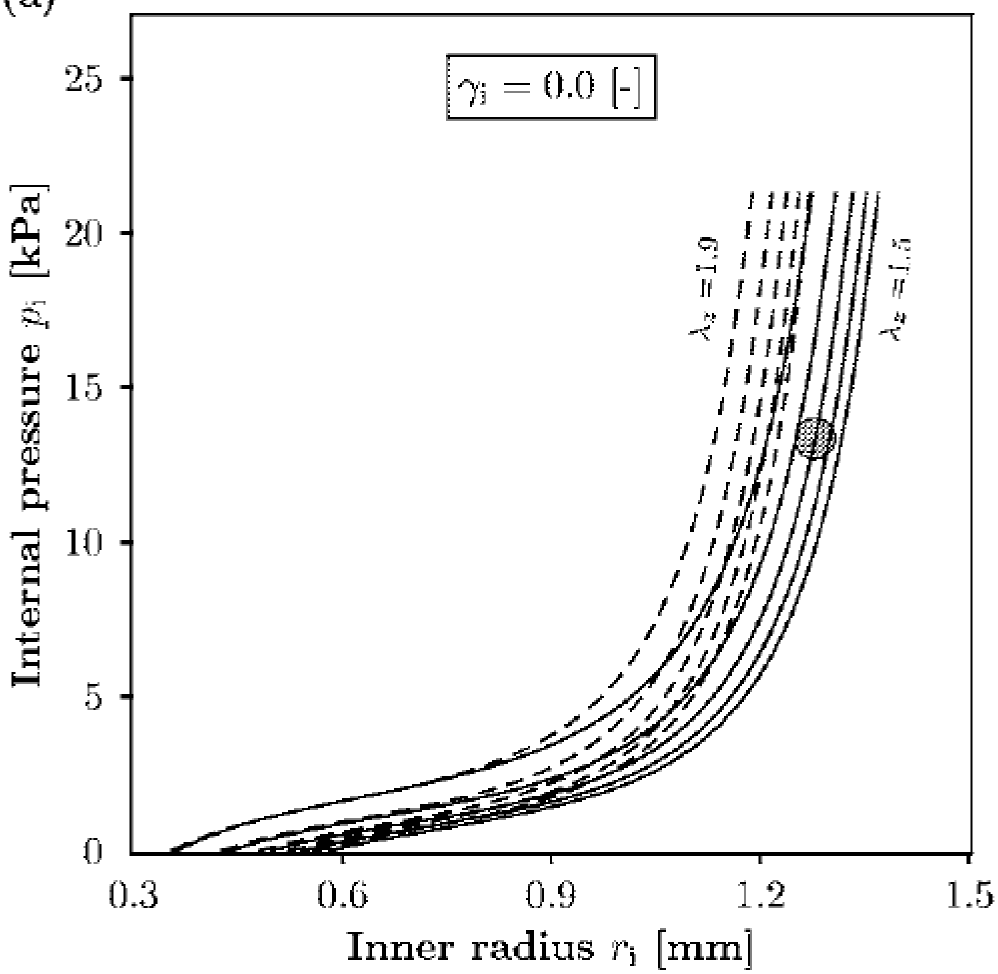

Figure 4.2: Pressure-inner radius curves for rabbit carotid artery during inflation are plotted at different stretch ratios from 1.5 to 1.9 without shear deformation (γ_i=0). Solid lines are numerical results obtained by using Gaussian quadrature with 3 nodes with residual strains included (Θ_0=100^0) and the dashed lines are results without residual strains (Θ_0=180^0) [15].

Table 4.1. Inner radius values of rabbit carotid artery at 13.33 kPa and 15 kPa computed by using 6 nodes are compared with values obtained (digitized from pressure-inner radius graph) by using 3 nodes [15] without and with residual strains, respectively.

	Inner Radius at 13.33 kPa [mm]		Inner Radius at 15 kPa [mm]	
	without resiudal stresses	with residual stresses	without residual stresses	with residual stresses
6 nodes	1.135	1.206	1.149	1.232
3 nodes	1.190	1.270	1.205	1.297

Figure 4.2 shows the same stress distributions computed by using 6 and 3 nodes at different inner radius values both for without and with residual strains. Inner radius values of rabbit carotid artery without and with residual strains computed by using 6 nodes do not greatly differ from its corresponding counters computed by using 3 nodes at the same pressure (Table 4.1). However, as it can be seen from Figure 4.3, stresses computed by using 6 nodes are almost two times greater than those computed by using 3 nodes at the same inner radius values digitized from the pressure-inner radius graph in Figure 4.2.

In conclusion, small differences in inner radius values result in large errors in stress values as the errors propagate through highly nonlinear media. Note that, the order of correctness is related to the number of nodes by "2n-1". Thus using 6 nodes gives the results with the correctness in the 11^{th} order whereas using 6 nodes gives 5^{th} order. It shows that 5^{th} order correctness is not sufficient to obtain correct stresses values using inner radius values in the order of [mm].

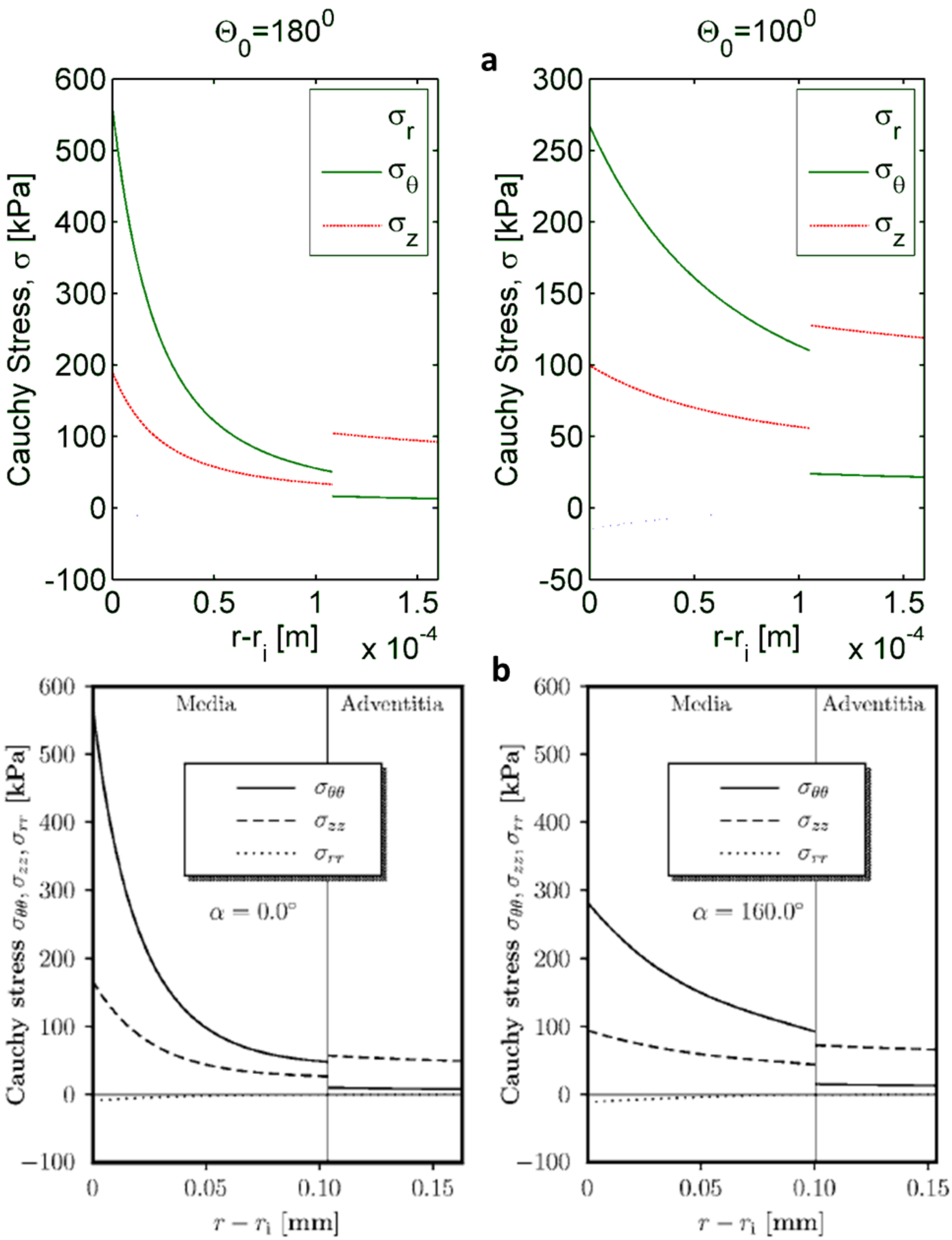

Figure 4.3: The same level of Cauchy stresses through the wall of the rabbit carotid artery are plotted by using Gaussian quadrature with (a) 6 nodes and with (b) 3 nodes [15] at different values of the inner radius according to the Table 4.1 without residual stresses ($\Theta_0=180^0$) and with residual stresses ($\Theta_0=100^0$), respectively .

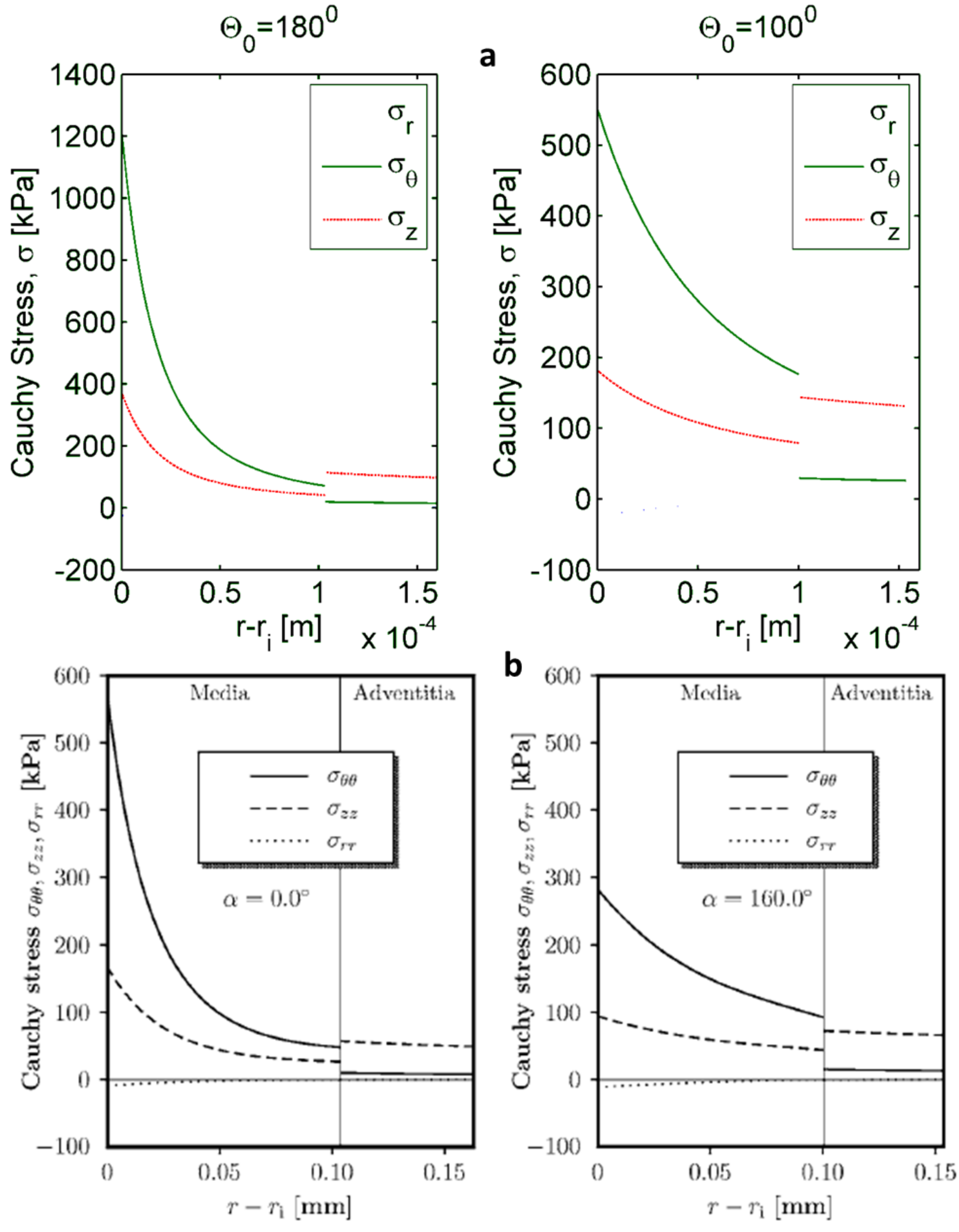

Figure 4.4: Cauchy stresses through the wall of the rabbit carotid artery are plotted by using Gaussian quadrature with (a) 6 nodes and with (b) 3 nodes [15] at the values of the inner radius computed by using 3 nodes without residual strains (Θ_0=180^0) and with residual strains (Θ_0=100^0), respectively.

4.2. Uniform Stress Distribution in Arteries

The main purpose of this chapter is to present vascular optimization scenarios in which the most uniform stress distribution through the arterial thickness is obtained by using two different approaches; 1. Remodeling-based and 2. Growth-based optimization of the arterial tissue.

The objective function is defined as the root-mean-square deviation of Cauchy stress components at final pressure $p+\Delta p$ from homeostatic stress components at initial pressure p .

$$\min\left\|\vec{\sigma}_f - \vec{\sigma}_{avg,in}\right\|_2 = \sqrt{\sum_{l=M,A}\sum_{k=rr,\theta\theta,zz} w_{k,l}\left(\frac{\sigma_{f,k,l}-\sigma_{avg,in,k,l}}{\sigma_{avg,in,k,l}}\right)^2} \tag{4.37}$$

where $\vec{\sigma}_{avg,in}$ is the homeostatic stress vector field in initial state and $\vec{\sigma}_f$ is the Cauchy stress vector field in final 1. remodeled or 2. grown state, and $w_{k,l}$ are weighting factors.

Homeostatic stresses are defined as the average of stresses through the arterial wall in initial state as given by

$$\sigma_{avg,in,k,l} = \frac{\int_{r_{i,l}}^{r_{o,l}} \sigma_{in,k,l}(2\pi r)dr}{\pi\left(r_{o,l}^2 - r_{i,l}^2\right)} \quad \text{for } k = rr,\theta\theta,zz \text{ and } l = M,A \tag{4.38}$$

Weighting factors are given by

$$w_{k,l} = \left|\frac{\sigma_{avg,in,k,l}}{\max\left(\sigma_{avg,in,k,l}\right)}\right|^2 \qquad \text{for } k = rr,\theta\theta,zz \text{ and } l = M,A \tag{4.39}$$

Both computed homeostatic Cauchy stress components and corresponding weighting factors are given in Table 4.2.

Table 4.2. Homeostatic (average) stress components in radial, circumferential directions for human carotid artery are computed for media and adventitia, respectively. For this purpose, material parameters and sizes of human carotid artery are used [15]. Corresponding weighting factors are also computed.

	$\sigma_{avg,rr,M}$ [kPa]	$\sigma_{avg,\theta\theta,M}$ [kPa]	$\sigma_{avg,zz,M}$ [kPa]	$\sigma_{avg,rr,A}$ [kPA]	$\sigma_{avg,\theta\theta,A}$[kPa]	$\sigma_{avg,zz,A}$ [kPa]
Homeostatic stresses	-2.2162	170.0737	75.3039	-0.3615	45.8985	246.3255
Weighting factors	1.6981e-4	1.0000	0.1961	2.1538e-6	3.4720e-2	1.0000

4.2.1. Remodeling-based Optimization

Remodeling-based optimization refers to the possible physical optimization problem in which the artery tries to sustain stress distribution close to the homeostatic stresses at initial pressure p by altering its material properties as the blood pressure increases to $p+\Delta p$ preserving the volume of the arterial volume (no growth).

In this scenario, the initial and final pressure are $p_i = 13.33kPa$ and $p_f = 15kPa$, respectively, and unknown parameters to be determined are material parameters. Optimal material parameters are computed by minimizing the objective function given in the Eq.(4.37).

Table 4.3. Computed optimal material parameters at $p_f = 15kPa$ for media and adventitia, respectively, are compared with original material parameters at $p_i = 13.33kPa$ [15].

Material Type	c_M [kPa]	c_A [kPa]	k_{1M} [kPa]	k_{1A} [kPa]	k_{2M} [-]	k_{2A} [-]	β_M [deg.]	β_A [deg.]
Remodeled Human Carotid Artery at 15 kPa	3.0000	0.3073	2.3631	0.5551	0.6433	0.9290	31.2	62.7
Original Human Carotid Artery at 13.33 kPa	**3.0000**	**0.3000**	**2.3632**	**0.5620**	**0.8393**	**0.7112**	**29.0**	**62.0**

4.2.2. Growth-based Optimization

Conversely, growth-based optimization refers to the possible physical optimization problem in which the artery tries to sustain stress distribution close to the homeostatic stresses at initial pressure p by altering its sizes (geometry) as the blood pressure increases to $p+\Delta p$ where material parameters remain constant.

Similarly for the growth-based optimization, the initial and final pressure are $p_i = 13.33kPa$ and $p_f = 15kPa$, respectively, but unknown parameters to be determined are growth factors appearing in front of residual strain parameters $R_i, R_o, \Theta_0, \lambda_z$ (see Ch.2) and inner radius at loaded state r_i. Optimal values of these growth factors parameters are also computed by minimizing the objective function given in the Eq.(4.37).

Table 4.4. Computed optimal growth parameters and volumetric growth factor at $p_f = 15kPa$ for media and adventitia, respectively, are compared with original parameters at $p_i = 13.33kPa$.

Material Type	g_{rr} [-]	$g_{\theta\theta}$ [-]	g_{zz} [-]	G_V
Remodeled Human Carotid Artery at 15 kPa	1.0000	1.0494	1.0477	1.0995
Original Human Carotid Artery at 13.33 kPa	**1.00**	**1.00**	**1.00**	**1.00**

where g_{rr}, $g_{\theta\theta}$ and g_{zz} are growth factors in radial, circumferential and axial directions, respectively. G_V is the volumetric growth factor defined in the Eq.(4.42) below.
Coordinate transformations in cylindrical coordinates are defined for loaded and unloaded states in terms of growth factors, respectively.

$$r(t_f) = g_{rr} r(t_i),\ \theta(t_f) = g_{\theta\theta}\theta(t_i) \text{ and } z(t_f) = g_{zz} z(t_i)$$
$$R(t_f) = g_{rr} R(t_i),\ \Theta(t_f) = g_{\theta\theta}\Theta(t_i) \text{ and } Z(t_f) = g_{zz} Z(t_i) \tag{4.40}$$

where the artery is in its original state at t_i (initial time) and grown state at t_f (final time). To emphasize, deviations in total stress components from homeostatic stress components leads to the arterial growth as the blood pressure increases.

Therefore, the differential volumetric transformation in cylindrical coordinates can expressed in terms of the volumetric growth factor.

$$dV = (g_{rr}dr)(g_{\theta\theta}d\theta)(g_{zz}dz) = G_V dr d\theta dz \tag{4.41}$$

where

$$G_V = g_{rr}g_{\theta\theta}g_{zz} = \frac{V_f}{V_i} \tag{4.42}$$

4.2.3. Optimal Stress Distributions

Computed remodeled-state and grown-state stresses are compared with stresses in original-state at $p = 15kPa$ in Figure 4.5.

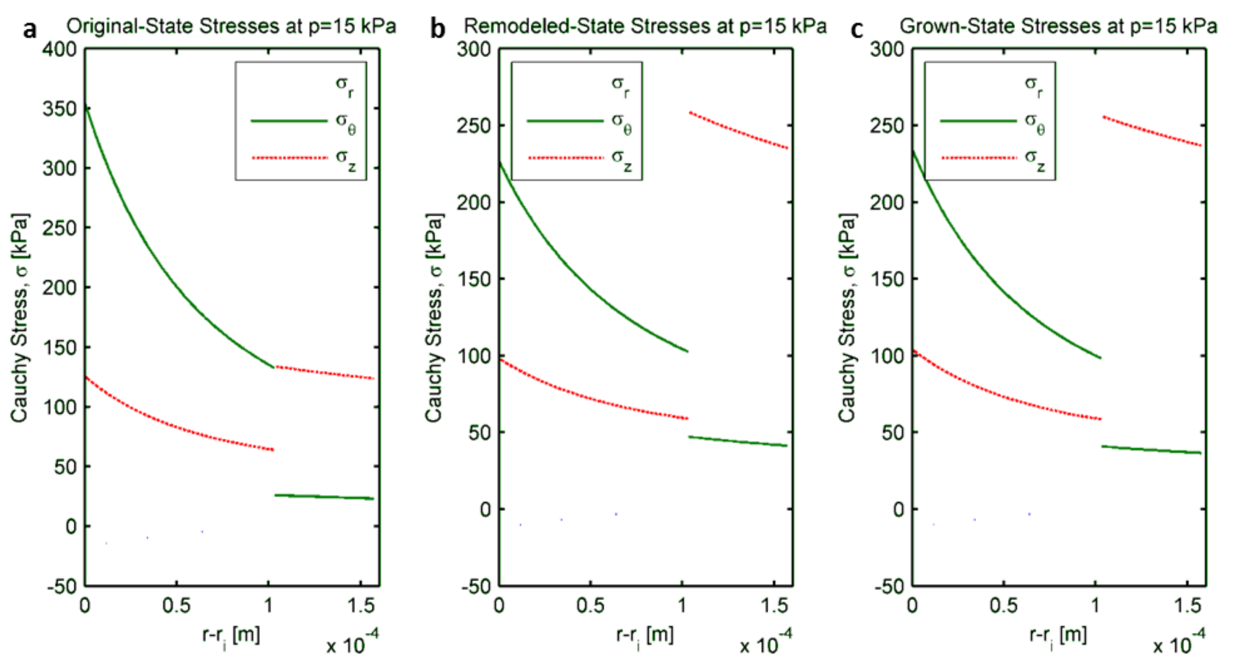

Figure 4.5: Cauchy stresses through the wall of the human carotid artery are plotted by using Gaussian quadrature with 6 nodes for (a) original-state (no remodeling and no growth), for (b) remodeled-state and for (c) grown-state with residual strains (Θ_0=100^0) at p=15 kPa, respectively.

As it can be seen from Figure 4.4, stresses computed both for remodeled-state and grown-state are almost the same. However, they significantly differ from the original-state stresses in magnitude. Therefore, it can be concluded that increased pressure may induce either remodeling (change in material parameters) or growth in order obtain the most possible uniform stress distribution depending on which one is less cost-effective.

Conclusion

All known techniques for estimating residual stresses are *invasive* and to our knowledge present technique is the first *non-invasive* methodology that can compute residual stress parameter *in vivo*, using standard clinical measurements. One of the additional message is that the residual stress distribution changes dramatically, while in vivo axial pre-stretch is present. The most striking point is that instead of performing *in vitro* experiments to measure residual strain parameters, it is merely sufficient to use the cuff pressure pressure-inner radius data obtained from diastolic-systolic pressure waveform by non-invasive clinical or biological measurement techniques in order to determine residual strains and stresses. Present technique can allow the prediction of local vessel growth due to an intended surgical intervention. Once residual strains and stresses are computed, stress-dependent finite growth models can be used to analyze the growth of vascular tissue belonging to specific patient. A segmental circumferential averaged formulation version can also allow the in vivo mapping of material properties as well as residual stresses along the vessel axis where properties are variable [85].

For linear elastic properties of vascular conduits that are examined, we have tested three commonly used biomedical conduits under biaxial tensile setup and measured their critical buckling twist angles under physiologically realistic pressure load. We demonstrate the linear relationships between critical buckling angle and blood pressure and also the direct corelation between newly defined coefficients $\kappa_1 = (\varphi_{cr} - c)/p$ and $\kappa_2 = (1+\nu)/E$ from the Eq.(3.5) due to the fact that the blood pressure is proportional to critical torque. On the other hand, significant difference (porcine pericardium almost 50 times stiffer) in the magnitude of stress-like parameter *c* appearing in Fung's 2D strain energy function between porcine pericardium and human pericardium suggests that the porcine pericardium is not a suitable material as vascular conduit since there is an enormous discontinuity in the stress field between boundaries of these two materials. Linear and nonlinear material properties suggest that the Dacron is the most durable conduit material to buckling while porcine pericardium is the worst one.

Results for remodeling-based and growth-based optimizations of human carotid artery show that both scenarios are appropriate to obtain the most uniform stress distribution close to homeostatic stresses. Long-term increase in the blood pressure may induce remodeling and/or growth in order to alleviate the stress level through the arterial wall. Therefore, assumptions of preconditioning and incompressibility are not sufficient any longer to estimate material properties of hyperelastic materials while stress-dependent growth and remodeling are present.

References

1. Whitlock, M.C. and W.G. Hundley, *Noninvasive Imaging of Flow and Vascular Function in Disease of the Aorta.* JACC Cardiovasc Imaging, 2015. **8**(9): p. 1094-106.
2. Fung, Y.C., *Biorheology of soft tissues.* Biorheology, 1973. **10**(2): p. 139-55.
3. Pinto, J.G. and Y.C. Fung, *Mechanical properties of the heart muscle in the passive state.* J Biomech, 1973. **6**(6): p. 597-616.
4. Lanir, Y. and Y.C. Fung, *Two-dimensional mechanical properties of rabbit skin. I. Experimental system.* J Biomech, 1974. **7**(1): p. 29-34.
5. Lanir, Y. and Y.C. Fung, *Two-dimensional mechanical properties of rabbit skin. II. Experimental results.* J Biomech, 1974. **7**(2): p. 171-82.
6. Fung, Y.C., *Stress, deformation, and atelectasis of the lung.* Circ Res, 1975. **37**(4): p. 481-96.
7. Tong, P. and Y.C. Fung, *The stress-strain relationship for the skin.* J Biomech, 1976. **9**(10): p. 649-57.
8. Vaishnav, R.N., et al., *Nonlinear anisotropic elastic properties of the canine aorta.* Biophys J, 1972. **12**(8): p. 1008-27.
9. Fung, Y.C., K. Fronek, and P. Patitucci, *Pseudoelasticity of arteries and the choice of its mathematical expression.* Am J Physiol, 1979. **237**(5): p. H620-31.
10. Chuong, C.J. and Y.C. Fung, *Three-dimensional stress distribution in arteries.* J Biomech Eng, 1983. **105**(3): p. 268-74.
11. Chuong, C.J. and Y.C. Fung, *On residual stresses in arteries.* J Biomech Eng, 1986. **108**(2): p. 189-92.
12. Takamizawa, K. and K. Hayashi, *Strain energy density function and uniform strain hypothesis for arterial mechanics.* J Biomech, 1987. **20**(1): p. 7-17.
13. Delfino, A., et al., *Residual strain effects on the stress field in a thick wall finite element model of the human carotid bifurcation.* J Biomech, 1997. **30**(8): p. 777-86.
14. Rachev, A. and S.E. Greenwald, *Residual strains in conduit arteries.* J Biomech, 2003. **36**(5): p. 661-70.
15. Holzapfel, G.A., T.C. Gasser, and R.W. Ogden, *A new constitutive framework for arterial wall mechanics and a comparative study of material models.* Journal of Elasticity, 2000. **61**(1-3): p. 1-48.
16. Donmazov, S., S. Piskin, and K. Pekkan, *Noninvasive in vivo determination of residual strains and stresses.* J Biomech Eng, 2015. **137**(6): p. 061011.
17. Bernal, M., et al., *Evaluation of Biaxial Mechanical Properties of Soft Tubes and Arteries using Sonometry.* 2009 Annual International Conference of the Ieee Engineering in Medicine and Biology Society, Vols 1-20, 2009: p. 2835-2838.
18. Zeinali-Davarani, S., et al., *Characterization of biaxial mechanical behavior of porcine aorta under gradual elastin degradation.* Ann Biomed Eng, 2013. **41**(7): p. 1528-38.
19. Han, H.C., *A biomechanical model of artery buckling.* J Biomech, 2007. **40**(16): p. 3672-8.
20. Han, H.C., *The theoretical foundation for artery buckling under internal pressure.* J Biomech Eng, 2009. **131**(12): p. 124501.
21. Lee, A.Y. and H.C. Han, *A Nonlinear Thin-Wall Model for Vein Buckling.* Cardiovasc Eng, 2010. **1**(4): p. 282-289.
22. Martinez, R., et al., *Mechanical buckling of veins under internal pressure.* Ann Biomed Eng, 2010. **38**(4): p. 1345-53.
23. Liu, Q., et al., *Artery buckling analysis using a four-fiber wall model.* Journal of Biomechanics, 2014. **47**(11): p. 2790-2796.
24. Garcia, J.R., S.D. Lamm, and H.C. Han, *Twist buckling behavior of arteries.* Biomech Model Mechanobiol, 2013. **12**(5): p. 915-27.
25. Han, H.C., et al., *Artery buckling: new phenotypes, models, and applications.* Ann Biomed Eng,

2013. **41**(7): p. 1399-410.
26. Hayman, D.M., et al., *Smooth muscle cell contraction increases the critical buckling pressure of arteries.* J Biomech, 2013. **46**(4): p. 841-4.
27. Lee, A.Y., et al., *Effects of elastin degradation and surrounding matrix support on artery stability.* Am J Physiol Heart Circ Physiol, 2012. **302**(4): p. H873-84.
28. Martinez, R. and H.C. Han, *The effect of collagenase on the critical buckling pressure of arteries.* Mol Cell Biomech, 2012. **9**(1): p. 55-75.
29. Beloussov, L.V., et al., *Mechanical stresses in embryonic tissues: patterns, morphogenetic role, and involvement in regulatory feedback.* Int Rev Cytol, 1994. **150**: p. 1-34.
30. Alford, P.W., J.D. Humphrey, and L.A. Taber, *Growth and remodeling in a thick-walled artery model: effects of spatial variations in wall constituents.* Biomechanics and Modeling in Mechanobiology, 2008. **7**(4): p. 245-262.
31. Alford, P.W. and L.A. Taber, *Computational study of growth and remodelling in the aortic arch.* Computer Methods in Biomechanics and Biomedical Engineering, 2008. **11**(5): p. 525-538.
32. Taber, L.A., *Theoretical study of Beloussov's hyper-restoration hypothesis for mechanical regulation of morphogenesis.* Biomech Model Mechanobiol, 2008. **7**(6): p. 427-41.
33. Taber, L.A., *Towards a unified theory for morphomechanics.* Philos Trans A Math Phys Eng Sci, 2009. **367**(1902): p. 3555-83.
34. Taber, L.A., *An optimization principle for vascular radius including the effects of smooth muscle tone.* Biophys J, 1998. **74**(1): p. 109-14.
35. Fung, Y.C., *What are the residual stresses doing in our blood vessels?* Annals of Biomedical Engineering, 1991. **19**(3): p. 237-249.
36. Frobert, O., et al., *Relation between zero-stress state and branching order of porcine left coronary arterial tree.* Am J Physiol, 1998. **275**(6 Pt 2): p. H2283-90.
37. Merodio, J., R.W. Ogden, and J. Rodríguez, *The influence of residual stress on finite deformation elastic response.* International Journal of Non-Linear Mechanics, 2013. **56**(0): p. 43-49.
38. Costa, M.F.M. and V. Teixeira, *Residual stress measurement in PVD optical coatings by microtopography.* Measurement, 2011. **44**(3): p. 549-553.
39. Scruby, C.B., et al., *Development of non-invasive methods for measurement of stress in welded steel structures : European Journal of Non-Destructive Testing, Vol. 3, No. 2, pp. 46–54 (Oct. 1992).* NDT & E International, 1996. **29**(2): p. 123.
40. Chuong, C.J. and Y.C. Fung, *On Residual Stresses in Arteries.* Journal of Biomechanical Engineering, 1986. **108**(2): p. 189-192.
41. Takamizawa, K. and K. Hayashi, *Strain energy density function and uniform strain hypothesis for arterial mechanics.* Journal of Biomechanics, 1987. **20**(1): p. 7-17.
42. Omens, J.H. and Y.C. Fung, *Residual strain in rat left ventricle.* Circ Res, 1990. **66**(1): p. 37-45.
43. Summerour, S.R., et al., *Residual strain in ischemic ventricular myocardium.* J Biomech Eng, 1998. **120**(6): p. 710-4.
44. Weis, S.M., et al., *Myocardial mechanics and collagen structure in the osteogenesis imperfecta murine (oim).* Circ Res, 2000. **87**(8): p. 663-9.
45. Liu, S.Q. and Y.C. Fung, *Influence of STZ-induced diabetes on zero-stress states of rat pulmonary and systemic arteries.* Diabetes, 1992. **41**(2): p. 136-46.
46. Pang, Q., et al., *Biomechanical properties of porcine cerebral bridging veins with reference to the zero-stress state.* J Vasc Res, 2001. **38**(1): p. 83-90.
47. Han, H.C. and Y.C. Fung, *Residual strains in porcine and canine trachea.* J Biomech, 1991. **24**(5): p. 307-15.
48. Xu, G., et al., *Opening angles and material properties of the early embryonic chick brain.* J Biomech Eng, 2010. **132**(1): p. 011005.
49. Taber, L.A., et al., *Residual strain in the ventricle of the stage 16-24 chick embryo.* Circ Res, 1993. **72**(2): p. 455-62.
50. Alford, P.W. and L.A. Taber, *Computational study of growth and remodelling in the aortic arch.* Comput Methods Biomech Biomed Engin, 2008. **11**(5): p. 525-38.

51. Wang, R. and R.L. Gleason, Jr., *A mechanical analysis of conduit arteries accounting for longitudinal residual strains.* Ann Biomed Eng, 2010. **38**(4): p. 1377-87.
52. Lu, X., et al., *Remodeling of the zero-stress state of femoral arteries in response to flow overload.* Am J Physiol Heart Circ Physiol, 2001. **280**(4): p. H1547-59.
53. Bischoff, J.E., E.A. Arruda, and K. Grosh, *A Microstructurally Based Orthotropic Hyperelastic Constitutive Law.* Journal of Applied Mechanics, 2002. **69**(5): p. 570-579.
54. Zhang, Y., et al., *A microstructural hyperelastic model of pulmonary arteries under normo- and hypertensive conditions.* Ann Biomed Eng, 2005. **33**(8): p. 1042-52.
55. Mekkaoui, C., et al., *Simultaneous measurements of arterial diameter and blood pressure to determine the arterial compliance, wall mechanics and stresses in vivo*. Eur J Vasc Endovasc Surg, 2001. **21**(3): p. 208-13.
56. Rodriguez, E.K., A. Hoger, and A.D. McCulloch, *Stress-dependent finite growth in soft elastic tissues.* J Biomech, 1994. **27**(4): p. 455-67.
57. Kowalski, W.J., et al., *Left atrial ligation alters intracardiac flow patterns and the biomechanical landscape in the chick embryo.* Developmental Dynamics, 2014. **243**(5): p. 652-662.
58. Restrepo, M., et al., *Fontan pathway growth: a quantitative evaluation of lateral tunnel and extracardiac cavopulmonary connections using serial cardiac magnetic resonance*. Ann Thorac Surg, 2014. **97**(3): p. 916-22.
59. Saugel, B., R. Dueck, and J.Y. Wagner, *Measurement of blood pressure.* Best Pract Res Clin Anaesthesiol, 2014. **28**(4): p. 309-322.
60. Naik, B.I. and M.E. Durieux, *Hemodynamic monitoring devices: Putting it all together.* Best Pract Res Clin Anaesthesiol, 2014. **28**(4): p. 477-488.
61. Quail, M.A., et al., *Development and validation of a novel method to derive central aortic systolic pressure from the MR aortic distension curve.* J Magn Reson Imaging, 2014. **40**(5): p. 1064-70.
62. Meidert, A.S., et al., *Radial artery applanation tonometry for continuous non-invasive arterial pressure monitoring in intensive care unit patients: comparison with invasively assessed radial arterial pressure.* Br J Anaesth, 2014. **112**(3): p. 521-8.
63. Janelle, G.M. and N. Gravenstein, *An accuracy evaluation of the T-Line Tensymeter (continuous noninvasive blood pressure management device) versus conventional invasive radial artery monitoring in surgical patients.* Anesth Analg, 2006. **102**(2): p. 484-90.
64. Szmuk, P., et al., *An evaluation of the T-Line Tensymeter continuous noninvasive blood pressure device during induced hypotension.* Anaesthesia, 2008. **63**(3): p. 307-12.
65. Meidert, A.S., et al., *Evaluation of the radial artery applanation tonometry technology for continuous noninvasive blood pressure monitoring compared with central aortic blood pressure measurements in patients with multiple organ dysfunction syndrome.* J Crit Care, 2013. **28**(6): p. 908-12.
66. Hong, H., et al., *Fontan conversion templates: patient-specific hemodynamic performance of the lateral tunnel versus the intraatrial conduit with fenestration.* Pediatr Cardiol, 2013. **34**(6): p. 1447-54.
67. Kowalski, W.J., et al. *Simultaneous real-time quantification of blood flow and vascular growth in the chick embryo using optical coherence tomography*. in *SPIE BiOS*. 2014. International Society for Optics and Photonics.
68. Lindsey, S.E., et al., *Growth and hemodynamics after early embryonic aortic arch occlusion.* Biomech Model Mechanobiol, 2014.
69. Roy, C.S., *The Elastic Properties of the Arterial Wall.* The Journal of Physiology, 1881. **3**(2): p. 125-159.
70. Fung, Y.C., *Biomechanics: Motion, Flow, Stress and Growth*. 1990: Springer.
71. Chuong, C.J. and Y.C. Fung, *COMPRESSIBILITY AND CONSTITUTIVE EQUATION OF ARTERIAL-WALL IN RADIAL COMPRESSION EXPERIMENTS.* Journal of Biomechanics, 1984. **17**(1): p. 35-40.
72. Humphrey, J.D., *Cardiovascular Solid Mechanics: Cells, Tissues, and Organs*. 2002: Springer.
73. Peña, E., et al., *A constitutive formulation of vascular tissue mechanics including viscoelasticity and*

softening behaviour. Journal of Biomechanics, 2010. **43**(5): p. 984-989.

74. Gasser, T.C., R.W. Ogden, and G.A. Holzapfel, *Hyperelastic modelling of arterial layers with distributed collagen fibre orientations.* Journal of The Royal Society Interface, 2006. **3**(6): p. 15-35.
75. Zulliger, M.A. and N. Stergiopulos, *Structural strain energy function applied to the ageing of the human aorta.* J Biomech, 2007. **40**(14): p. 3061-9.
76. Garcia-Herrera, C.M., D.J. Celentano, and E.A. Herrera, *Modelling and numerical simulation of the in vivo mechanical response of the ascending aortic aneurysm in Marfan syndrome.* Med Biol Eng Comput, 2016.
77. Sommer, G., et al., *Mechanical strength of aneurysmatic and dissected human thoracic aortas at different shear loading modes*. Journal of Biomechanics.
78. Vande Geest, J.P., et al., *Towards A Noninvasive Method for Determination of Patient-Specific Wall Strength Distribution in Abdominal Aortic Aneurysms.* Annals of Biomedical Engineering, 2006. **34**(7): p. 1098-1106.
79. Monson, K.L., N.M. Barbaro, and G.T. Manley, *Biaxial Response of Passive Human Cerebral Arteries.* Annals of biomedical engineering, 2008. **36**(12): p. 2028-2041.
80. Salacinski, H.J., et al., *The Mechanical Behavior of Vascular Grafts: A Review*. Journal of Biomaterials Applications, 2001. **15**(3): p. 241-278.
81. Hasegawa, M. and T. Azuma, *Mechanical properties of synthetic arterial grafts.* Journal of Biomechanics. **12**(7): p. 509-517.
82. Lucereau, B., et al., *Relation between tensile tests and compliance in polyester textile vascular prostheses.* Ann Vasc Surg, 2015. **29**(6): p. 1300-6.
83. Bustos, C.A., C.M. Garcia-Herrera, and D.J. Celentano, *Mechanical characterisation of Dacron graft: Experiments and numerical simulation.* J Biomech, 2016. **49**(1): p. 13-8.
84. Shafigh, M., N. Fatouraee, and A. Seddighi, *Fung's Model Constants for Intracranial Blood Vessel of Human Using Biaxial Tensile Test Results.*
85. Maher, E., et al., *Site specific inelasticity of arterial tissue.* J Biomech, 2012. **45**(8): p. 1393-9.